Journal of Computational Physics (2020)

Contents lists available at ScienceDirect

Journal of Computational Physics

journal homepage: www.elsevier.com/locate/jcp

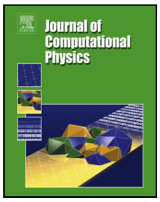

Optimization of Multidimensional Diagonal-Norm Summation-by-Parts Operators on Simplices

André L. Marchildon[a,*], David W. Zingg[a,1]

[a] *Institute for Aerospace Studies, University of Toronto, 4925 Dufferin St., Toronto, ON, Canada*

ARTICLE INFO

Article history:
Received Day Month 2019
Received in final form Day Month Year
Accepted Day Month Year
Available online Day Month Year

Communicated by A. L. Marchildon

Finite-difference methods
Summation-by-parts
Unstructured grid

ABSTRACT

This paper investigates the construction and optimization of multidimensional summation-by-parts (SBP) operators. The optimization of free parameters in the cubature rule, the interpolation/extrapolation operator R, and in the skew-symmetric matrix S_ξ, is investigated and a methodology to optimize the operators is presented. It is demonstrated that increasing the degree of the cubature rule from $2p-1$ to $2p$, where p is the degree of the operator, is beneficial to minimizing the solution error. The optimization method developed is applied to construct novel multidimensional SBP operators on triangular and tetrahedral elements. For example, new operators with collocated element and facet cubature nodes are constructed with fewer element nodes and with lower solution errors. For instance, the $p=2$ operator has 10 fewer element nodes and a solution error 44% to 68% lower for the same computational cost than the previous best operator of the same degree and family.

1. Introduction

Summation-by-parts (SBP) operators are finite-difference operators that are readily applicable to higher order methods with provable stability for linear and nonlinear problems from their construction designed to mimic integration by parts [1, 2]. The original SBP operators, now commonly referred to as classical SBP operators, are built on one-dimensional operators and are extended to higher dimensions using a tensor-product formulation. The classical SBP operators have an element node on each of the boundaries and also have boundary stencils and repeating interior stencils. It is possible to construct classical SBP operators with norm matrices, H, that are either diagonal or dense. The former has been utilized to a larger extent since it was proven early on to be stable on curvilinear grids [3], while the latter has only recently been proven stable [4]. SBP operators were generalized by Del Rey Fernández *et al.* [5] to allow for non-repeating interior stencils, non-uniform nodal distributions, and to remove the need to have element nodes on the boundaries. The operators utilizing these additional properties are referred to as generalized

---

[*] Corresponding author: email: andre.marchildon@mail.utoronto.ca

[1] Email: dwz@utias.utoronto.ca

SBP operators. These generalizations enable element-type operators and multidimensional operators [6, 7] applicable to unstructured grids and arbitrary polyhedra.

The construction of SBP operators begins with quadrature and cubature rules of degree $2p-1$ or greater, where p is the degree of the operator [8]. In one dimension, integrals are approximated by quadrature rules, which are well known and extensively utilized [9]. Examples of quadrature rules include Legendre-Gauss (LG), which is the family of quadrature rules of the highest degree for a given number of nodes, and Legendre-Gauss-Lobatto (LGL), which is the family of quadrature rule of the highest degree for a given number of nodes with nodes on the boundaries. In multiple dimensions, quadrature rules are commonly called cubature rules. Unlike in one dimension, where equations exist to derive quadrature rules of arbitrary degree, the development of cubature rules often depends on numerical methods [10]. This process involves solving for the weight and nodal locations using an objective function that includes the difference between the exact integration of basis functions over the element and the numerical integration. A cubature rule of a given degree is found once the objective function that contains all basis functions of a given degree evaluates to zero. Several examples of cubature rules found in this way can be found in [11, 12, 13, 14].

The number of degrees of freedom (DOF) and equations that need to be considered when solving for cubature rules can be reduced by having all of the nodes in symmetry groups. Liu and Vinokur [15] developed a set of equations to derive cubature rules of degree one to five on simplices of one to three dimensions with all of the nodes in symmetry groups. These equations indicate the minimum required number of DOF to have a cubature rule of a given degree.

Another aspect that needs to be considered when determining the nodal locations for the cubature rule is the interpolation/extrapolation of the solution from element to facet cubature nodes for imposition of boundary and interface conditions. A valid cubature rule can be constructed if the nodes are evenly spaced in the domain. However, the interpolant for a set of evenly spaced nodes is susceptible to the Runge phenomenon [9]. A measure of the quality of the interpolation for a set of nodes is the Lebesgue constant, which provides an upper bound on the interpolation error using the L_∞ norm [16]. A lower Lebesgue constant is desirable and the set of nodes with the minimum Lebesgue constant are referred to as the Lebesgue nodes.

In the construction of SBP and other high-order schemes there are often free parameters that remain after operators are constructed with the required properties. Various objective functions have been used to optimize these free parameters, including the Lebesgue constant, the spectral radius, and the bandwidth [17, 18]. Several studies investigating the optimization of SBP operators have considered only one-dimensional operators [17, 19] and recently, multidimensional SBP elements have been considered as well [20, 21]. In the 2014 study by Mattsson *et al.*, the nodal locations of the one-dimensional element boundary nodes for SBP operators were optimized [19]. It was found that changing the nodal locations from the starting equidistant element nodes to optimized nodal locations reduced the solution error in some cases by an order of magnitude.

In addition to SBP operators, flux reconstruction operators have also been optimized. These schemes construct a flux that is continuous across the element and its interfaces [22]. A 2014 study investigated the impact of different cubature rules on triangular elements for a flux reconstruction scheme [18]. This study determined that the operators that provide the lowest solution error for an isentropic vortex test case have cubature rules of higher degree as well as lower Lebesgue constants than the other operators. This study demonstrated the importance for element nodal locations to have both good integration and interpolation properties.

Witherden *et al.* later studied the importance of cubature rules for flux reconstruction schemes with tetrahedral elements [23]. In this case, two different test cases were used, which both involved the Euler equations, and a set of progressively finer meshes was used. Hundreds of cubature rules were derived and used with both test cases. It was found that the cubature rules that provided the minimum solution error for one test case did not necessarily have the minimum solution error for the other test case. However, it was found that the flux reconstruction operators with the lowest solution error for one test case also always had a low solution error for the other test case.

The first objective of this paper is to determine how to optimize the free parameters in the SBP operators such that solution error is minimized. The next objective is to identify the SBP operators that provide the lowest solution error for a given computational cost for various SBP families, which are introduced in Section 3.3. The SBP operators are constructed using different cubature rules, and all of their free parameters are optimized using the methodology that is found to provide the optimal operators.

2. Notation

The notation presented in this section is based on [6]. Capital letters with script type denote continuous functions. For instance, $\mathcal{U}(x, y) \in C^{\infty}(\Omega)$ is an infinitely differentiable function of two variables in the domain Ω. Meanwhile, functions that are evaluated at a set of nodes are identified by lowercase bold fonts. For example, the evaluation of $\mathcal{U}(x, y)$ on a set of nodes is given by $\boldsymbol{u} = [\mathcal{U}(x_1, y_1), \ldots, \mathcal{U}(x_n, y_n)]^T$.

Monomial basis functions are used in this paper to avoid cumbersome Taylor series and to simplify the proofs. However, in the construction of SBP operators a basis function that does not become ill-conditioned as quickly as monomials should be used, such as the Legendre polynomials. The cardinality of basis functions is indicated by $N^*_{p,d}$, where p indicates the order of the operator and d is the number of dimensions. The cardinality for one to three dimensions evaluates to $N^*_{p,0} = 1$, $N^*_{p,1} = p + 1$, $N^*_{p,2} = (p + 1)(p + 2)/2$, and $N^*_{p,3} = (p + 1)(p + 2)(p + 3)/6$. To facilitate the reference to monomial basis functions a single index notation is used:

$$\mathcal{P}_k(\xi, \eta) \equiv \xi^i \eta^{j-i}, \quad k = \frac{j(j+1)}{2} + i + 1, \quad \forall j \in \{0, 1, \ldots, p\}, \quad i \in \{0, 1, \ldots, j\}.$$

The k-th basis function and its ξ derivative evaluated at the element nodes is given by

$$\begin{aligned} \boldsymbol{p}_k &\equiv [\mathcal{P}_k(\xi_1, \eta_1), \ldots, \mathcal{P}_k(\xi_n, \eta_n)]^T, \\ \boldsymbol{p}'_k &\equiv \left[\frac{\partial \mathcal{P}_k}{\partial \xi}(\xi_1, \eta_1), \ldots, \frac{\partial \mathcal{P}_k}{\partial \xi}(\xi_n, \eta_n) \right]^T. \end{aligned}$$

The combination of these basis functions can be used to form a Vandermonde matrix of degree p along with a matrix that holds the ξ derivative of the monomial basis functions

$$\begin{aligned} \mathsf{V} &= [\boldsymbol{p}_1, \ldots, \boldsymbol{p}_{N^*_{p,d}}], \\ \mathsf{V}_\xi &= [\boldsymbol{p}'_1, \ldots, \boldsymbol{p}'_{N^*_{p,d}}]. \end{aligned}$$

The physical element and its boundaries are denoted by Ω and Γ, respectively, and the physical coordinates are $(x, y, z) \in \Omega$. Meanwhile, the computational element and its boundaries are denoted by $\hat{\Omega}$ and $\hat{\Gamma}$, respectively, and their coordinates are $(\xi, \eta, \zeta) \in \hat{\Omega}$.

Element nodes refer to nodes at which the solution is evaluated, while facet nodes are those where the facet integration is performed. DOF indicate all of the entries in a matrix that can be used to satisfy a set of equations, while the free parameters are the entries that remain unspecified in the matrices after some of the DOF have been used to satisfy a set of equations. The number of element nodes is indicated by n, while the number of facet nodes is given by n_f.

3. Multidimensional summation-by-parts operators

3.1. Definition of a summation-by-parts operator

A d-dimensional SBP operator is defined as [6]:

Definition 1. ***A d-dimensional summation-by-parts operator:*** *The square matrix D_ξ is a degree p approximation to the first derivative $\frac{\partial}{\partial \xi}$ on the set of element nodes $S_{\hat{\Omega}}$ for an open and bounded domain $\hat{\Omega} \in \mathbb{R}^d$ with a piecewise linear boundary if*

1. $\mathsf{D}_\xi \boldsymbol{p}_k = \boldsymbol{p}'_k, \quad \forall k \in \{1, 2, \ldots, N^*_{p,d}\}$;
2. $\mathsf{D}_\xi = \mathsf{H}^{-1}\mathsf{Q}_\xi$, where H is symmetric positive-definite; and
3. $\mathsf{Q}_\xi = \mathsf{S}_\xi + \frac{1}{2}\mathsf{E}_\xi$, where $\mathsf{S}^T_\xi = -\mathsf{S}_\xi$, $\mathsf{E}^T_\xi = \mathsf{E}_\xi$, and E_ξ satisfies:

$$\boldsymbol{p}_k^T \mathsf{E}_\xi \boldsymbol{p}_m = \oint_{\hat{\Gamma}} \mathcal{P}_k \mathcal{P}_m n_\xi d\hat{\Gamma}, \quad \forall k, m \in \{1, 2, \ldots, N^*_{p,d}\},$$

where n_ξ is the ξ component of the unit outward pointing normal on $\hat{\Gamma}$.

The matrix H is commonly referred to as the norm matrix since it approximates a cubature rule of degree $p_{\text{cub}} \geq 2p-1$ and it defines a finite-dimensional norm. When H is diagonal, which is the only case considered in this paper, then all the entries must be positive in order to have a positive-definite matrix.

With this definition, SBP operators mimic integration by parts term by term:

$$\underbrace{\int_{\hat{\Omega}} \mathcal{V}\frac{\partial \mathcal{U}}{\partial \xi} d\hat{\Omega}}_{\boldsymbol{v}^T \mathsf{H}\mathsf{D}_{\xi}\boldsymbol{u}} + \underbrace{\int_{\hat{\Omega}} \mathcal{U}\frac{\partial \mathcal{V}}{\partial \xi} d\hat{\Omega}}_{\boldsymbol{u}^T \mathsf{H}\mathsf{D}_{\xi}\boldsymbol{v}} = \underbrace{\oint_{\hat{\Gamma}} \mathcal{V}\mathcal{U} n_{\xi} d\hat{\Gamma}}_{\boldsymbol{v}^T \mathsf{E}_{\xi}\boldsymbol{u}}, \tag{1}$$

which can also be cast as the compatibility equations

$$\mathsf{V}^T \mathsf{H}\mathsf{V}_{\xi} + \mathsf{V}_{\xi}^T \mathsf{H}\mathsf{V} = \mathsf{V}^T \mathsf{E}_{\xi}\mathsf{V}. \tag{2}$$

3.2. Construction of summation-by-parts operators

This section presents a methodology for the construction of one-dimensional or multidimensional SBP operators with diagonal norm matrices. Section 5 will introduce a method to construct optimized SBP operators. The first step in the construction of SBP operators with diagonal norm matrices is to use either an existing cubature rule or to construct a cubature rule of degree $p_{\text{cub}} \geq 2p-1$ with exclusively positive weights. In this paper, only cubature rules with all of the element nodes within the element are considered. Section 3.4 will provide further details on the construction of cubature rules, particularly when all of the nodes are in symmetry groups.

Once the nodal locations and the norm matrix H have been set by the cubature rule, the next step is to create the interpolation/extrapolation operator R_j, which is for facet j and is of degree $r \geq p$. The operator R_j is constructed to satisfy

$$\mathsf{R}_j \mathsf{V}_{\hat{\Omega}} = \mathsf{V}_{\hat{\Gamma}}, \tag{3}$$

where $\mathsf{V}_{\hat{\Omega}}$ and $\mathsf{V}_{\hat{\Gamma}}$ are the Vandermonde matrices for the element and facet nodes of degree p and r, respectively. The operator R_j can be calculated as [7]

$$\mathsf{R}_j = \mathsf{V}_{\hat{\Gamma}_j}(\mathsf{V}_{\hat{\Omega}})^{\dagger}, \tag{4}$$

where $(\cdot)^{\dagger}$ is the Moore-Penrose pseudoinverse, which in this case requires the columns of $\mathsf{V}_{\hat{\Omega}}$ to be linearly independent such that Eq. (3) is satisfied. The matrix E_{ξ} can be constructed as:

$$\mathsf{E}_{\xi} = \sum_{j=1}^{N_{\hat{\Gamma}}} n_{\xi,j} \mathsf{R}_j^T \mathsf{B}_j \mathsf{R}_j, \tag{5}$$

where $N_{\hat{\Gamma}}$ is the number of facets, $\mathsf{B}_j = \operatorname{diag}(b_1^{(j)}, \dots b_{n_j}^{(j)})$, which is a cubature rule of at least degree $2p$, and $n_{\xi,j}$ is the contribution of the normal vector in the ξ direction for facet j. It was shown in [7] that Eq. (5) satisfies the third condition from Definition 1.

The construction of S_{ξ} requires matrices W and W_{ξ} to be of size $n \times (n - N_{p,d}^*)$ in order to form the following square matrices

$$\tilde{\mathsf{V}} = [\mathsf{V}\,\mathsf{W}], \tag{6}$$

$$\tilde{\mathsf{V}}_{\xi} = [\mathsf{V}_{\xi}\,\mathsf{W}_{\xi}], \tag{7}$$

where the square brackets indicate concatenation of the matrices. The columns in the matrix W must also be selected to be linearly independent to those of V such that $\tilde{\mathsf{V}}$ is invertible. When $n = N_{p,d}^*$, W and W_{ξ} are empty. The DOF in S_{ξ} are used to satisfy the first condition from Definition 1, which is referred to as the accuracy conditions. To solve for S_{ξ}, we begin with the accuracy conditions and use the second and third conditions from Definition 1 to find

$$\mathsf{S}_{\xi} = \mathsf{H}([\mathsf{V}_{\xi}\,\mathsf{W}_{\xi}])\,([\mathsf{V}\,\mathsf{W}])^{-1} - \frac{1}{2}\mathsf{E}_{\xi}. \tag{8}$$

It was shown in [7] that the DOF in W_{ξ} can be used to ensure S_{ξ} is skew-symmetric and that the accuracy conditions are satisfied. Another method of solving for S_{ξ} will be presented in Section 5.5, where the independent equations will be identified such that S_{ξ} can be solved with free parameters that can be used to optimize the SBP operator.

Table 1: Primary symmetry groups for simplices.

			Line		Triangle		Tetrahedron	
Sym group	Description	DOF	n	$\frac{n}{\text{DOF}}$	n	$\frac{n}{\text{DOF}}$	n	$\frac{n}{\text{DOF}}$
s_{cent}	Centroid	1	1	1	1	1	1	1
$\text{s}_{\text{c-vert}}$	Vertex cent.	2	2	1	3	1.5	4	2
$\text{s}_{\text{c-edge}}$	Edge cent.	3			6	2	12	4
$\text{s}_{\text{c-mid-edge}}$	Mid-edge cent.	2					6	3
$\text{s}_{\text{c-face}}$	Face cent.	4					24	6

3.3. Classification of multidimensional summation-by-parts operators

Multidimensional SBP operators can be classified into different sets of families. Three families have been previously introduced in [7, 24], which were designed as the Ω, Γ and diagonal-E families. A more general classification for SBP families is introduced where the three families are R^d, R^{d-1} and R^0.

The Ω family was originally defined in [7] to designate operators with strictly interior element nodes. This means that none of the element nodes for the operator can be on the facets. For these operators, all of the element nodes are used to interpolated/extrapolate the solution to the facet nodes. Hence, the interpolation/extrapolation of the solution spans d dimensions. One limitation of this family is that none of the element nodes can be on the facets. This limitation is removed for the newly defined SBP family R^d. This family is defined as the operators whose interpolation/extrapolation spans d dimensions. Therefore, all of the Ω operators fall within the R^d family. An operator will be presented in Section 6.1.1 that is in the R^d family but not in the Ω family since it has element nodes on the facets.

The Γ family was originally defined for triangular elements to have $p + 1$ element nodes on each facet [7]. When this requirement is generalized to arbitrary d, it requires $N^*_{p,d-1}$ element nodes on each facet. This number of element nodes on each facet reduces the dimensionality of the interpolation/extrapolation by one, that is, the interpolation/extrapolation spans $d - 1$ dimensions instead of the d for the R^d family. This means that only the element nodes on a facet are used to interpolate/extrapolate the solution to the facet nodes on that facet. The R^{d-1} family is similar to the Γ family but instead of requiring exactly $N^*_{p,d-1}$ element nodes on each facet, it requires at least $N^*_{p,d-1}$ element nodes on each facet. Therefore, all of the Γ operators will also be R^{d-1} operators.

The diagonal-E family was first presented in [24] and it requires each facet node to be collocated with an element node. This collocation of the nodes leads to a diagonal matrix E_ξ, hence the name of the family. However, an SBP operator with a diagonal matrix E_ξ that does not have collocated facet and element nodes would not be in the diagonal-E family, which makes this family name somewhat misleading. For example, the one-dimensional $p = 1$ SBP operator that is constructed with the two-node LG quadrature rule has a diagonal E_ξ matrix. Yet, its facet nodes are not collocated with its element nodes, which makes it a part of the Ω family and not the diagonal-E family. The new family name that is introduced is R^0, which indicates that the interpolation/extrapolation spans zero dimensions. This clearly indicates that each facet node is collocated with an element node. The diagonal-E and R^0 families are equivalent since they both require the collocation of the facet and element nodes.

3.4. Construction of symmetric cubature rules

In this paper only SBP operators with symmetric cubature rules are used. The symmetry groups for simplices of one to three dimensions are shown in Table 1. When constructing cubature rules, it is helpful to use symmetry groups with a smaller n/DOF ratio since they provide more DOF to the cubature rule, which allows the operator to be further optimized without adding additional nodes.

For the R^{d-1} and R^0 families, a certain number of element nodes need to be on the facets to reduce the dimensionality of the interpolation/extrapolation. Table 2 provides the symmetry groups for the simplices of one to three dimensions that have their nodes on the facets. The symmetry groups with element nodes on the facets are degenerate symmetry groups from Table 1 with at least one fewer DOF since one DOF in the nodal locations is used to have the element nodes on the facets. The different symmetry groups for triangles and tetrahedra are shown in Figs. 1 and 2, respectively. The symmetry groups with a ‘c’ in their subscript indicates the nodes are on a line or plane that is centered between the vertices, edges or mid-edges. For example, the symmetry group $\text{s}_{\text{c-vert}}$ has its nodes on the lines

Table 2: Symmetry groups for simplices that have the element nodes on the facets.

Groups on facets	Nodal locations	Primary group	Facet equiv. group	line	tri	tet
s_{vert}	On the vertices	$s_{\text{c-vert}}$	s_{vert}	✓	✓	✓
s_{edge}	On the edges	$s_{\text{c-edge}}$	$s_{\text{c-vert}}$(line) s_{edge}(tri)		✓	✓
$s_{\text{mid-edge}}$	On the mid-edges	$s_{\text{c-vert}}$(tri) $s_{\text{c-mid-edge}}$(tet)	$s_{\text{mid-edge}}$		✓	✓
$s_{\text{face-cent}}$	Cent. of the faces	$s_{\text{c-vert}}$	s_{cent}			✓
$s_{\text{c-face-vert}}$	Faces vertex cent.	$s_{\text{c-edge}}$	$s_{\text{c-vert}}$			✓
s_{face}	On the faces	$s_{\text{c-face}}$	$s_{\text{c-edge}}$			✓

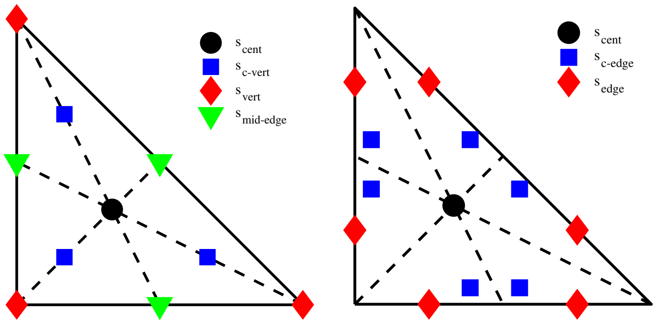

(a) Vertex centered (b) Edge centered

Fig. 1. Nodal symmetry groups for triangles.

that originate from the vertices and continue to the opposing facet's centroid. The symmetry group s_{vert} meanwhile, has its nodes at the vertices specifically. Therefore, s_{vert} is a subset of the $s_{\text{c-vert}}$ symmetry group.

Liu and Vinokur [15] investigated the construction of cubature rules algebraically for simplices with all of the nodes in symmetry groups. Table 3 indicates the number of DOF that are required to have a cubature rule of degree one to five for lines, triangles and tetrahedra. This information is used to create new cubature rules for SBP operators in Sections 6 and 7.

4. Construction of operators with free parameters

In Section 3.2 a method to construct SBP operators was presented but it does not result in any free parameters. In this section, a different method of constructing SBP operators is presented such that they have free parameters that can be optimized for various objective functions, which will be introduced in Section 5.1. Section 4.1 will discuss how directional operators and the interpolation/extrapolation operator R can be permuted such that they only need to be constructed for one direction and facet, respectively. Next, Section 4.2 will demonstrate that R_1 needs to be constructed with additional constraints than those presented in Section 3.2 in order for the SBP operators to have the proper decomposition when the matrix E_η is constructed by permuting E_ξ. Finally, Section 4.3 will demonstrate how the independent accuracy equations can be identified.

4.1. Permutation of the operators

Using the permutation matrices from Appendix A.1, the directional operators such as D_ξ only need to be constructed in one direction and can then be permuted to the other directions. Similarly, only R_1 needs to be constructed since the interpolation/extrapolation for the other facets can be found by permuting R_1. The advantage of only constructing the directional operators for one direction and the interpolation/extrapolation operator for one facet is that they only need to be optimized once. Furthermore, the permutation of the operators ensures that they have exactly the same properties in each direction.

The reference triangular and tetrahedral elements are shown in Fig. 3. The vertices of the reference elements are on the axes and a unit length away from the origin, e.g. vertex II is at coordinate (1,0) in Fig. 3a. The reference triangle is a right triangle, while the reference tetrahedron is a trirectangular tetrahedron, i.e. a tetrahedron with three

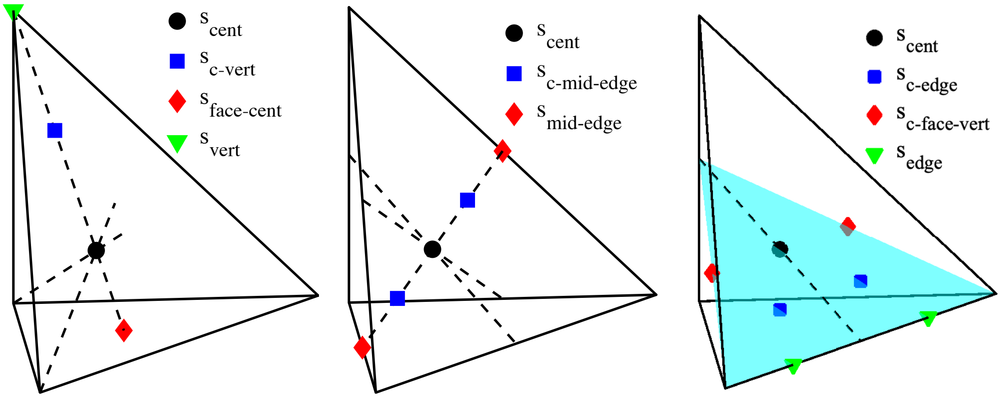

(a) Vertex centered (b) Mid-edge centered (c) Edge centered

Fig. 2. Nodal symmetry groups along one vertex, mid-edge, or edge for tetrahedra.

Table 3: Minimum required number of DOF to have a cubature rule of degree one to five on a simplex element with nodes in symmetry groups.

	Required number of DOF				
p_{cub}	1	2	3	4	5
Line	1	2	2	3	3
Triangle	1	2	3	4	5
Tetrahedron	1	2	3	5	6

right triangles for its facets. The notation that is used has the first vertex at the origin and then each one is in the same order as the coordinates, i.e. ξ, η and then ζ. The facets share the same number as the vertex they face.

Theorem 1. *For a simplex reference element, such as the ones shown in Fig. 3, the directional operator* D_η *can be found by permuting the operator* D_ξ *as follows:*

$$\mathsf{D}_\eta = \mathsf{P}_{\xi-\eta}\mathsf{D}_\xi\mathsf{P}_{\xi-\eta}. \tag{9}$$

where $\mathsf{P}_{\xi-\eta}$ *is the permutation matrix for the symmetry line or plane where* $\xi = \eta$.

Proof: The proof can be found in Appendix A.2.

Similarly, it can be shown that other directional operators can be permuted in the same way

$$\mathsf{S}_\eta = \mathsf{P}_{\xi-\eta}\mathsf{S}_\xi\mathsf{P}_{\xi-\eta} \tag{10}$$

$$\mathsf{E}_\eta = \mathsf{P}_{\xi-\eta}\mathsf{E}_\xi\mathsf{P}_{\xi-\eta} \tag{11}$$

$$\mathsf{Q}_\eta = \mathsf{P}_{\xi-\eta}\mathsf{Q}_\xi\mathsf{P}_{\xi-\eta}. \tag{12}$$

Permuting the directional operators to the ζ direction for a tetrahedral operator is analogous. Similarly, the interpolation/extrapolation operators only need to be constructed for one facet and can then be permuted to each of the other facets.

Theorem 2. *A triangular SBP operator can have its operator* R_2 *constructed by permuting* R_1 *as follows:*

$$\mathsf{R}_2 = \mathsf{R}_1\mathsf{P}_{r:1-2}. \tag{13}$$

where $\mathsf{P}_{r:1-2} = \mathsf{P}_1\mathsf{P}_3$ *for the triangular reference element shown in Fig. 3a.*

Proof: The proof is in Appendix A.3.

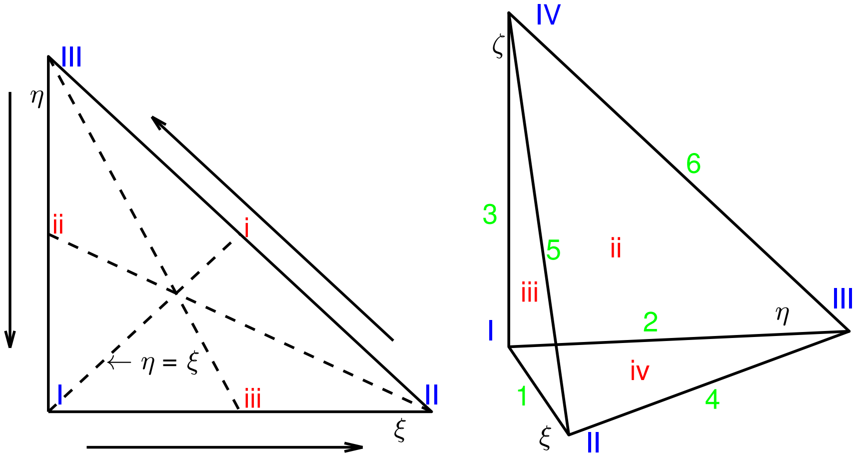

(a) Reference triangular element

(b) Reference tetrahedral element (facet *i* is bounded by vertices *II*, *III* and *IV*)

Fig. 3. Reference simplex elements where lowercase Roman numerals indicate facet numbers, uppercase Roman numerals indicate vertex numbers, arrows on the triangular element indicate the direction in which the facets are evaluated, and the green numbers are for the local edge numbers on the tetrahedral element.

4.2. Symmetry conditions on the construction of R

In previous multidimensional SBP papers, Eq. (4) was used to construct the interpolation/extrapolation operator R_1, which is fine if E_η and E_ζ are constructed using equations similar to Eq. (5). However, when the operators E_η and E_ζ are constructed by permuting E_ξ, additional restrictions on the construction of R_1 are required for E_η and E_ζ to have the proper decomposition into R_1, as detailed in

Theorem 3. *The operator* R_1 *must be constructed to ensure that the contribution of element nodes to the interpolation/extrapolation of the solution to the facet nodes is equal across symmetry lines and planes such that the directional operators* E_η *and* E_ζ *that are constructed from permuting* E_ξ *have the proper decomposition into* R_1.

Proof: The proof is in Appendix B.

Fig. 4 shows the requirements of Theorem 3 for the contributions of the interpolation/extrapolation of the solution from element to facet nodes for a triangular element. Similarly, Fig. 5 shows the interpolation/extrapolation contribution from element to facet nodes for a tetrahedral operator. The element nodes in Fig. 5 are on the facet for clarity but the result would be the same if they were in the element instead. As the proof to Theorem 3 in Appendix B demonstrates, the requirement for the contributions of the interpolation/extrapolation to be symmetric across symmetry lines and planes does not require additional DOF in R_1, since there is also a reduction in the number of independent equations that need to be considered due to the symmetry. Therefore, when all of the element and facet nodes are in symmetry groups, there is always a solution with symmetric contributions across symmetry lines in R_1 as long as Eq. (4) returns a valid solution, which requires that the columns of $\mathsf{V}_{\hat{\Omega}}$ be linearly independent. Appendix C provides a set of modified Moore-Penrose pseudoinverse equations that ensures the contributions from the interpolation/extrapolation are symmetric about all symmetry lines and planes.

4.3. Skew-symmetric matrix S_ξ

To satisfy the accuracy equations from Definition 1, a total of $n \times N^*_{p,d}$ equations must be satisfied. However, since S_ξ is skew-symmetric, there are only $n(n-1)/2$ DOF available to satisfy all of these equations. Therefore, there are often more equations than unknowns. This has previously been identified and it has been demonstrated that it is possible to satisfy all of the equations [6]. However, this previous method does not allow free parameters to remain. A new method is introduced that identifies the independent equations that need to be considered, which allows the system of equations to be solved with free parameters that can be used for the optimization. The first step is to recast

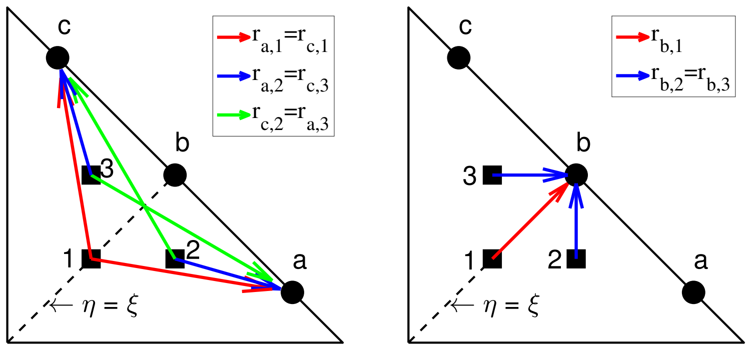

(a) Contributions to the facet $s_{\text{c-vert}}$ nodes

(b) Contributions to the facet s_{cent} node

Fig. 4. Symmetric contributions to the interpolation/extrapolation operator R_1 from element nodes to facet nodes.

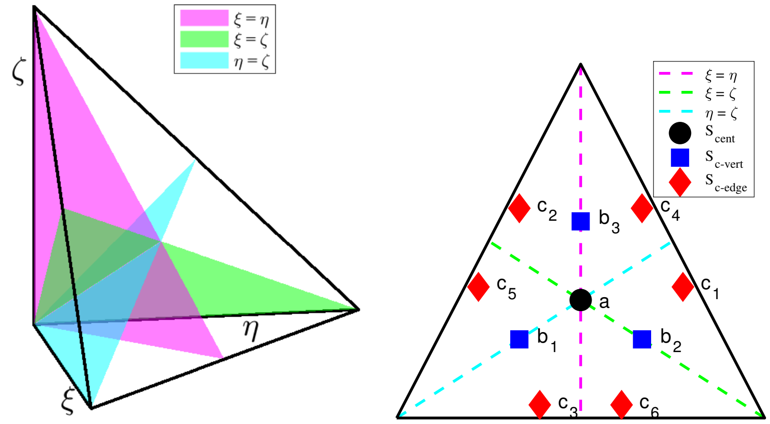

(a) Symmetry planes that intersect facet i

(b) Facet i with the symmetry planes and the facet symmetry groups

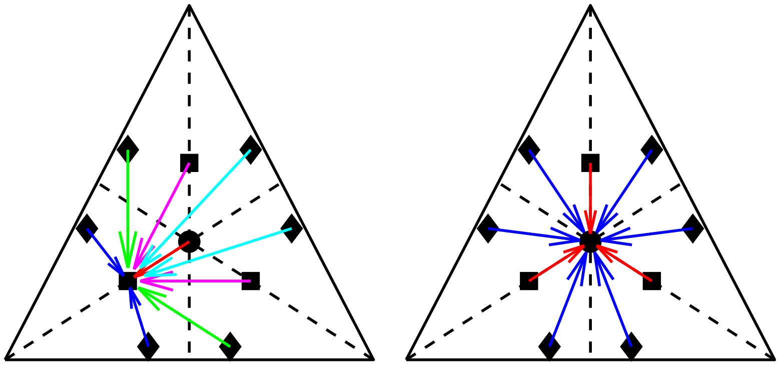

(c) Interpolation/extrapolation contributions from element nodes to one $s_{\text{c-vert}}$ facet node

(d) Interpolation/extrapolation contributions from element nodes to the s_{cent} facet node

Fig. 5. Symmetric contributions to the interpolation/extrapolation operator R_1 from element nodes to facet nodes for a tetrahedral element.

the accuracy conditions into the form

$$\mathsf{S}_\xi \mathsf{V} = \mathsf{H}\mathsf{V}_\xi - \frac{1}{2}\mathsf{E}_\xi \mathsf{V}. \tag{14}$$

Both sides of Eq. (14) are of size $n \times N^*_{p,d}$, which is the number of equations that need to be satisfied for the accuracy equations. To identify a smaller set of equations that are independent, Eq. (14) is left multiplied by $\tilde{V}^T = [\mathsf{V}\,\mathsf{W}]^T$:

$$[\mathsf{V}\,\mathsf{W}]^T \mathsf{S}_\xi \mathsf{V} = [\mathsf{V}\,\mathsf{W}]^T \left(\mathsf{H}\mathsf{V}_\xi - \frac{1}{2}\mathsf{E}_\xi \mathsf{V} \right). \tag{15}$$

Eq. (15) can be separated into two distinct equations

$$\mathsf{V}^T \mathsf{S}_\xi \mathsf{V} = \mathsf{V}^T \mathsf{H}\mathsf{V}_\xi - \frac{1}{2}\mathsf{V}^T \mathsf{E}_\xi \mathsf{V}, \tag{16}$$

$$\mathsf{W}^T \mathsf{S}_\xi \mathsf{V} = \mathsf{W}^T \mathsf{H}\mathsf{V}_\xi - \frac{1}{2}\mathsf{W}^T \mathsf{E}_\xi \mathsf{V}. \tag{17}$$

Eq. (2) can be substituted into Eq. (16) for $\mathsf{V}^T \mathsf{E}_\xi \mathsf{V}$ to obtain

$$\mathsf{V}^T \mathsf{S}_\xi \mathsf{V} = \frac{1}{2}(\mathsf{V}^T \mathsf{H}\mathsf{V}_\xi - \mathsf{V}_\xi^T \mathsf{H}\mathsf{V}). \tag{18}$$

Both sides of Eq. (18) are matrices of size size $N^*_{p,d} \times N^*_{p,d}$. However, since both sides are skew-symmetric, there are only $N^*_{p,d}(N^*_{p,d} - 1)/2$ independent equations.

For Eq. (17) all of the $(n - N^*_{p,d}) \times N^*_{p,d}$ equations need to be considered. Therefore, there are a total of

$$n_{\mathsf{S}_\xi \text{ind eq}} = \frac{N^*_{p,d}(N^*_{p,d} - 1)}{2} + (n - N^*_{p,d})N^*_{p,d} = \frac{N^*_{p,d}(2n - N^*_{p,d} - 1)}{2} \tag{19}$$

independent equations from Eqs. (16) and (17). The number of free parameters that remain in S_ξ after Eqs. (16) and (17) are satisfied is

$$n_{\mathsf{S}_\xi \text{FP}} = DOF - n_{\mathsf{S}_\xi \text{ind eq}} = \frac{(n - N^*_{p,d})(n - N^*_{p,d} - 1)}{2}, \tag{20}$$

which is never negative since $n \geq N^*_{p,d}$. Eq. (20) indicates that there will only be free parameters in S_ξ when $n > N^*_{p,d} + 1$. The free parameters in S_ξ can be used to create a sparse matrix, or they can be used to optimize the operator for various objective functions, which will be investigated in Section 5.5.

Eq. (20) is applicable to element based one-dimensional operators as well as multidimensional operators. However, this equation is not directly applicable to classical SBP operators since these have a specific structure with boundary stencils of degree p and $2p - 1$ for diagonal and dense norm operators, respectively, and repeating interior stencils of degree $2p$. To derive Eq. (20), it was only assumed that S_ξ is skew-symmetric, while classical SBP operators have the additional requirement that S_ξ is in a particular form to have the needed boundary and repeating interior stencils.

5. Optimization of free parameters in the operators

In Section 4 a methodology was developed to construct SBP operators with free parameters. This section investigates the optimization of these free parameters. Section 5.1 introduces the objective functions that are used and then Section 5.2 presents the test cases that are used to evaluate the properties of the different optimized operators. In the construction of SBP operators there can be free parameters in the cubature rule, R_1, and S_ξ; these are investigated in Sections 5.3, 5.4 and 5.5, respectively.

5.1. Objective functions

In the investigation of the optimization of the free parameters in the cubature rule, R_1 and in S_ξ various objective functions are used. To investigate the optimization of free parameters in the cubature rule, the error in the element integration is used as an objective to be minimized

$$e_{\text{elem-int}} = \sqrt{\sum_{k=N^*_{p_{\text{cub}},d}+1}^{N^*_{p_{\text{cub}}+1,d}} \left(\mathbf{1}^T \mathsf{H} \boldsymbol{p}_k - I_{\hat{\Omega},k} \right)^2}, \tag{21}$$

where $I_{\hat{\Omega},k}$ is the exact integration of the k-th basis function over the reference element $\hat{\Omega}$, and $\mathbf{1}$ is a vector of ones of length n. When there are sufficient free parameters in the cubature rule, it is possible to increase the degree of the cubature rule by reducing $e_{\text{elem-int}}$ to zero. This objective function, as well as the next one, are calculated using monomial basis functions.

The H norm of the leading truncation error terms is another potentially important quantity to minimize:

$$e_{\text{derivative}} = \sqrt{\sum_{k=N^*_{p,d}+1}^{N^*_{p+1,d}} (\mathsf{D}_\xi \boldsymbol{p}_k - \boldsymbol{p}'_k)^T \mathsf{H} (\mathsf{D}_\xi \boldsymbol{p}_k - \boldsymbol{p}'_k)}, \tag{22}$$

where the indices for the polynomials used in Eqs. (21) and (22) were selected such that only polynomials one degree higher than the maximum degree that can be exactly integrated or differentiated were used for the respective objective functions.

The Frobenius norm of a matrix is a helpful objective function since it bounds the spectral radius of a matrix [25]:

$$\rho(\mathsf{A}) \leq \|\mathsf{A}\|_F, \tag{23}$$

where $\rho(\mathsf{A})$ is the spectral radius of the matrix A, and the Frobenius norm of a matrix with real entries is calculated as

$$\|\mathsf{A}\|_F = \sqrt{\text{Tr}(\mathsf{A}^T\mathsf{A})} = \sqrt{\sum_{i=1}^{m_1}\sum_{j=1}^{m_2} a_{i,j}^2}, \tag{24}$$

where m_1 and m_2 indicate the size of the matrix A, and the trace operator, which takes the sum of diagonal entries in a matrix, is given by Tr. When the problem is stability limited and an explicit time marching scheme is used, the spectral radius is important since the size of the time step is limited by the spectral radius of the global SBP operator, i.e. the operator that is created by combining the contributions from all of the individual elements and their SATs. Therefore, global operators with smaller Frobenius norm have a smaller spectral radius and thus a larger time step can be used, which reduces the computational cost. Using the Frobenius norm as an objective function instead of the spectral radius directly is advantageous since the former is differentiable, which makes its minimization easier. It is the spectral radius of the global operator that is important, but it is infeasible to optimize the free parameters using the global operator since it becomes problem dependent and the global operator can also be very large. Instead, the Frobenius norm of the matrix A is minimized, which is defined as

$$\mathsf{A} = \mathsf{D}_\xi + \mathsf{R}_1^T \mathsf{B}_1 \mathsf{R}_1. \tag{25}$$

The matrix A combines the element derivative operator D_ξ and also a contribution from the SATs. It will be shown in Section 5.4 that the minimization of the Frobenius norm of A is preferable over simply the minimization of the Frobenius norm of D_ξ.

5.2. Test cases

Test cases are used to investigate the optimization of free parameters and to compare different optimized operators with respect to the error in the solution. A linear convection test case is presented in Section 5.2.1 that is used for the triangular and tetrahedral operators. Section 5.2.2 then presents two different test cases for the two- and three-dimensional operators based on the Euler equations governing inviscid compressible fluid flow. For the two-dimensional test cases, a mesh with quadrilaterals is first created and each element is then divided into two triangles. For the three-dimensional test cases, a mesh with hexahedral elements is created and each element is then divided into six tetrahedra. The meshes are then curved according to the mesh transformation presented in Section 5.2.3. Periodic boundary conditions are used for all the test cases.

SBP operators provide provable stability for linear problems such as the linear convection equation. Provable nonlinear stability with SBP operators is achieved by using entropy stable fluxes [28]. While entropy stable fluxes were not used for the test cases considered in this paper, the numerical solutions were nonetheless found to be stable for the nonlinear test case considered based on the Euler equations.

For all of the test cases upwind SATs and the fourth-order Runge-Kutta method are used. The time step is set to

$$\Delta t = \frac{\text{CFL}\,\Delta x}{v_{\text{char}}}, \tag{26}$$

where v_{char} is the characteristic speed, which is problem dependent, CFL is the Courant-Friedrichs-Lewy number, and Δx is the length of one quadrilateral or hexahedral element before the mesh curvature. All of the quadrilateral or hexahedral elements are squares and cubes, respectively, and thus the use of Δy or Δz instead of Δx would provide the same result. Unless indicated otherwise in the figure captions, the CFL number is set to 0.01 and 0.05 for the two- and three-dimensional test cases, respectively. These small CFL numbers ensure that the error from the temporal discretization is negligible relative to the error from the spatial discretization.

The solution error for the test cases is quantified using the broken-H norm, which is defined as

$$\sqrt{||\boldsymbol{u}||^2_{\mathsf{H}_g}} = \sqrt{\sum_{i=1}^{K} ||\boldsymbol{u}_i||^2_{\mathsf{H}}}, \tag{27}$$

where H_g is the global SBP norm matrix and K is the number of elements in the mesh. It is important to note that the matrix H for each element needs to be scaled by the appropriate mapping Jacobian since elements are typically of different sizes.

The discrete energy of the system is given by $\boldsymbol{u}^T \mathsf{H}_g \boldsymbol{u}$. As such, the change in the discrete energy of the system is calculated as

$$\Delta \mathrm{E} = \boldsymbol{u}_0^T \mathsf{H}_g \boldsymbol{u}_0 - \boldsymbol{u}^T \mathsf{H}_g \boldsymbol{u}. \tag{28}$$

5.2.1. Linear convection test cases

The three-dimensional linear convection equation is

$$\frac{\partial \mathcal{U}}{\partial t} + \frac{\partial a_x \mathcal{U}}{\partial x} + \frac{\partial a_y \mathcal{U}}{\partial y} + \frac{\partial a_z \mathcal{U}}{\partial z} = 0, \tag{29}$$

where a is the constant velocity in the direction indicated by the subscript. The domain $\Omega \subset \mathbb{R}^3$ is discretized into K non-overlapping elements $\bar{\Omega} = \cup_{k=1}^{K} \bar{\Omega}_k$ and $\Omega_i \cap \Omega_j = \emptyset, \forall i \neq j$. Each element is then mapped to computational space

$$\frac{\partial \mathcal{J}^{-1} \mathcal{U}}{\partial t} + \frac{\partial a_\xi \mathcal{U}}{\partial \xi} + \frac{\partial a_\eta \mathcal{U}}{\partial \eta} + \frac{\partial a_\zeta \mathcal{U}}{\partial \zeta} = 0, \tag{30}$$

where $\mathcal{J}$ is the metric Jacobian of the transformation, $a_\xi = \mathcal{J}^{-1}(\xi_x + \xi_y + \xi_z)$, $a_\eta = \mathcal{J}^{-1}(\eta_x + \eta_y + \eta_z)$, $a_\zeta = \mathcal{J}^{-1}(\zeta_x + \zeta_y + \zeta_z)$, ξ_x represents $\frac{\partial \xi}{\partial x}$ and similarly for the other terms of this form. The initial solution for the test case is

$$u_0 = \exp\left(-\frac{x^2 + y^2 + z^2}{2\sigma^2}\right), \tag{31}$$

where $\sigma = 0.1$ and the Cartesian domain is $[0,1] \times [0,1] \times [0,1]$. The test case is stopped once the wave returns to its initial position. The velocities are set to $a_x = a_y = a_z = 0.5$, which is the characteristic speed and it means the final time is $t = 2$. The two-dimensional test case is recovered by dropping all the terms that contain z or ζ.

5.2.2. Euler equations test cases

The two-dimensional isentropic vortex test case from [26] is used with a Cartesian domain $[0,20] \times [-5,5]$ with a uniform mesh (before it is curved) and an analytical solution given by

$$\rho = \left(1 - \frac{(\gamma - 1)\left(\beta e^{1 - r(\boldsymbol{x},t)^2}\right)^2}{16\gamma\pi^2}\right)^{\frac{1}{\gamma - 1}}, \tag{32}$$

$$p = \rho^\gamma, \tag{33}$$

$$u = 1 - \frac{\beta e^{1 - r(\boldsymbol{x},t)^2}(y - y_0)}{2\pi}, \tag{34}$$

$$v = \frac{\beta e^{1 - r(\boldsymbol{x},t)^2}(x - x_0 - t)}{2\pi}, \tag{35}$$

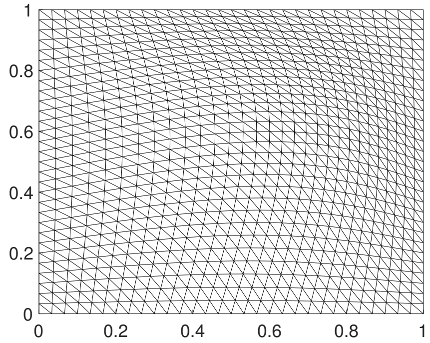

Fig. 6. Curved two-dimensional mesh with $30 \times 30 \times 2 = 1800$ **triangular elements.**

where $x_0 = 5, y_0 = 0, \beta = 5$ and $r(\boldsymbol{x}, t) = \sqrt{(x - x_0 - t)^2 + (y - y_0)^2}$. The characteristic speed that is used to calculate the time step in Eq. (26) is the speed at which the vortex moves across the domain, which is unity. The vortex travels from $(x_0, y_0) = (5, 0)$ to $(15, 0)$.

For the three-dimensional test case, source terms are selected such that a manufactured solution that is infinitely differentiable and smooth satisfies the equations. The manufactured solution is

$$\rho = 2 + \frac{\sin(2\pi(x + y + z - 2t))}{10}, \tag{36}$$

$$u = v = w = 1, \tag{37}$$

$$e = 5, \tag{38}$$

where the characteristic speed is thus unity and the source terms are

$$s_\rho = \frac{\pi}{5}\cos(2\pi(x + y + z - 2t)), \tag{39}$$

$$s_{\rho u} = s_{\rho v} = s_{\rho w} = -\frac{\pi(3\gamma - 5)}{10}\cos(2\pi(x + y + z - 2t)), \tag{40}$$

$$s_e = -\frac{9\pi(\gamma - 1)}{10}\cos(2\pi(x + y + z - 2t)). \tag{41}$$

5.2.3. *Curvilinear mesh*

The mesh is constructed on the Cartesian domain $[0, 1] \times [0, 1] \times [0, 1]$ and then curved according to the following transformation

$$\begin{aligned} x' &\leftarrow x + a\cos(\pi(x - 0.5))\cos(\pi(y - 0.5))\cos(\pi(z - 0.5)), \\ y' &\leftarrow y + a\cos(\pi(x - 0.5))\cos(\pi(y - 0.5))\cos(\pi(z - 0.5)), \\ z' &\leftarrow z + a\cos(\pi(x - 0.5))\cos(\pi(y - 0.5))\cos(\pi(z - 0.5)), \end{aligned}$$

where $a = 1/10$ and $a = 1/20$ for the two- and three-dimensional problems, respectively. For the two-dimensional problems, the terms with z are dropped. An example of a curved mesh is shown in Fig. 6.

The metric invariants for SBP operators are only exactly satisfied if the degree of the mapping is less than or equal to $p + 1$ and $\left\lfloor \frac{p}{2} \right\rfloor + 1$ in two and three dimensions, respectively [28]. As such, the metric invariants for curvilinear meshes with $p = 1$ operators are only satisfied exactly if the degree of the curvature is limited to two and one for two- and three-dimensional operators, respectively. For three-dimensional operators, it is possible to solve an optimization problem to have a polynomial mapping of degree $p+1$ [28]. However, this was not utilized. As such, the degree of the polynomial mapping for $p = 1$ and $p = 2$ operators is limited to two and one for two- and three-dimensional operators, respectively. This means that for triangular elements the location of the vertices and mid-edges are set according to the mesh curvature and the rest of the element is curved according to a second-order polynomial mapping. For tetrahedral operators, only the vertices are set according to the mesh curvature and the rest of the operator is found with a linear mapping. The meshes are isoparametric, i.e. the degrees of the operators and of the polynomial mapping of the meshes are equal, for the $p = 2$ operators in two dimensions and the $p = 1$ operators in three dimensions.

5.3. *Optimizing free parameters in the cubature rule*

Simple operators with one and two free parameters in the cubature rule are investigated to determine which objective function should be used to optimize these free parameters. Two- and three-dimensional examples will be provided to demonstrate that the same conclusions can be drawn for triangular and tetrahedral operators.

5.3.1. *Operator with $p = 1$ and $n = N^*_{1,d}$*

The simplest multidimensional operator that can be considered has $p = 1$ with $n = N^*_{1,2} = 3$. The symmetry group $\mathrm{s}_{\text{c-vert}}$ is used, which has two DOF in the cubature rule as indicated in Table 1. One DOF is used to enforce the minimum cubature rule degree of $2p - 1 = 1$ and the SBP operators on a triangle are

$$S_{\hat{\Omega}} = \begin{bmatrix} \frac{1-t_1}{3} & \frac{1-t_1}{3} \\ \frac{2t_1+1}{3} & \frac{1-t_1}{3} \\ \frac{1-t_1}{3} & \frac{2t_1+1}{3} \end{bmatrix}, \qquad \mathsf{R}_1 = \begin{bmatrix} \frac{t_1-1}{3t_1} & \frac{2t_1+\sqrt{3}+1}{6t_1} & \frac{2t_1-\sqrt{3}+1}{6t_1} \\ \frac{t_1-1}{3t_1} & \frac{2t_1-\sqrt{3}+1}{6t_1} & \frac{3t_1+\sqrt{3}+1}{6t_1} \end{bmatrix},$$

$$\mathsf{H} = \begin{bmatrix} \frac{1}{6} & 0 & 0 \\ 0 & \frac{1}{6} & 0 \\ 0 & 0 & \frac{1}{6} \end{bmatrix}, \qquad \mathsf{D}_\xi = \begin{bmatrix} -\frac{1}{t_1} & \frac{1}{t_1} & 0 \\ -\frac{1}{t_1} & \frac{1}{t_1} & 0 \\ -\frac{1}{t_1} & \frac{1}{t_1} & 0 \end{bmatrix}, \tag{42}$$

where t_1 is a free parameter for the nodal locations, and $-1/2 \leq t_1 \leq 1$ ensures that the element nodes are within the reference element, as shown in Fig. 7a. Similarly, the $\mathrm{s}_{\text{c-vert}}$ symmetry group can be used to construct a $p = 1$ tetrahedral operator with $p_{\text{cub}} = 2p - 1 = 1$, $n = N^*_{1,3} = 4$ and one free parameter for the cubature rule, which must be in the range $-1/3 \leq t_1 \leq 1$ to ensure all the nodes are within the element, as shown by Fig. 7c.

Figs. 7b and 7d show the solution errors, which are calculated using Eq. (27), and the values of various objective functions as the free parameter t_1 is varied for the two- and three-dimensional operators, respectively. From Figs. 7b and 7d, it is evident that the solution error is minimized for both the triangular and tetrahedral operators when $e_{\text{elem-int}}$ is zero, which indicates a cubature rule of degree $2p = 2$. There is a large gap in the solution when t_1 is near zero, which is the value at which all of the element nodes are collocated at the centroid. The gap in the solution error indicates that the operator is not stable for the size of the time step used. This coincides with high values of the Frobenius norm of A, indicating that the Frobenius norm of A is a good indicator of the spectral radius of the global operator matrix. The objective function $e_{\text{derivative}}$ is minimized as t_1 approaches zero, which is where the solution is unstable. Therefore, the leading truncation error is a poor objective function to use to optimize the free parameters in the cubature rule. This test was replicated with a coarser mesh and different CFL numbers and the results led to the same observations.

5.3.2. *Operator with $p = 1$ and $n = N^*_{1,d} + 1$*

To further demonstrate the benefit of using the free parameters in the cubature rule to increase the degree of the cubature rule, consider an operator with one $\mathrm{s}_{\text{c-vert}}$ symmetry group as well as the s_{cent} symmetry group. The operators for the triangular element with $p_{\text{cub}} = 2p - 1 = 1$ are

$$S_{\hat{\Omega}} = \begin{bmatrix} \frac{1}{3} & \frac{1}{3} \\ \frac{1-t_1}{3} & \frac{1-t_1}{3} \\ \frac{2t_1+1}{3} & \frac{1-t_1}{3} \\ \frac{1-t_1}{3} & \frac{2t_1+1}{3} \end{bmatrix}, \qquad \mathsf{R}_1 = \begin{bmatrix} r_1 & \frac{t_1-1}{3t_1} - \frac{r_1}{3} & \frac{2t_1+\sqrt{3}+1}{6t_1} - \frac{r_1}{3} & \frac{2t_1-\sqrt{3}+1}{6t_1} - \frac{r_1}{3} \\ r_1 & \frac{t_1-1}{3t_1} - \frac{r_1}{3} & \frac{2t_1-\sqrt{3}+1}{6t_1} - \frac{r_1}{3} & \frac{2t_1+\sqrt{3}+1}{6t_1} - \frac{r_1}{3} \end{bmatrix},$$

$$\mathsf{H} = \begin{bmatrix} \frac{1-3w_1}{2} & 0 & 0 & 0 \\ 0 & \frac{w_1}{2} & 0 & 0 \\ 0 & 0 & \frac{w_1}{2} & 0 \\ 0 & 0 & 0 & \frac{w_1}{2} \end{bmatrix}, \qquad \mathsf{D}_\xi = \begin{bmatrix} 0 & -\frac{1}{t_1} & \frac{1}{t_1} & 0 \\ -\frac{3w_1+r_1-1}{w_1 t_1} & \frac{r_1-1}{3w_1 t_1} & \frac{6w_1+r_1-1}{3w_1 t_1} & \frac{3w_1+r_1-1}{3w_1 t_1} \\ \frac{3w_1+r_1-1}{w_1 t_1} & -\frac{6w_1+r_1-1}{3w_1 t_1} & -\frac{r_1-1}{3w_1 t_1} & -\frac{3w_1+r_1-1}{3w_1 t_1} \\ 0 & -\frac{1}{t_1} & \frac{1}{t_1} & 0 \end{bmatrix}, \tag{43}$$

where w_1 is the weight on the $\mathrm{s}_{\text{c-vert}}$ symmetry group. The tetrahedral operators with the same symmetry group have a similar format. There are two free parameters in the cubature rule and one in the interpolation/extrapolation operator R_1. In order to investigate only the impact of the free parameters in the cubature rule, r_1 is set to zero, which means that the element centroid does not contribute to the interpolation/extrapolation of the solution to the facet nodes. Fig.

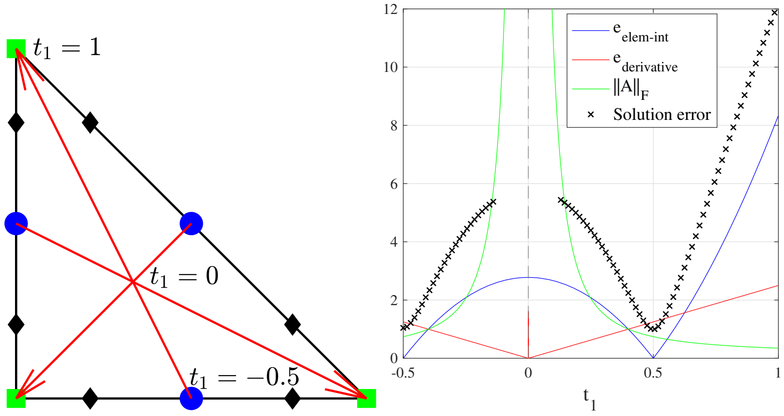

(a) Nodal locations for triangular element (b) Normalized solution error and objective functions using triangular elements

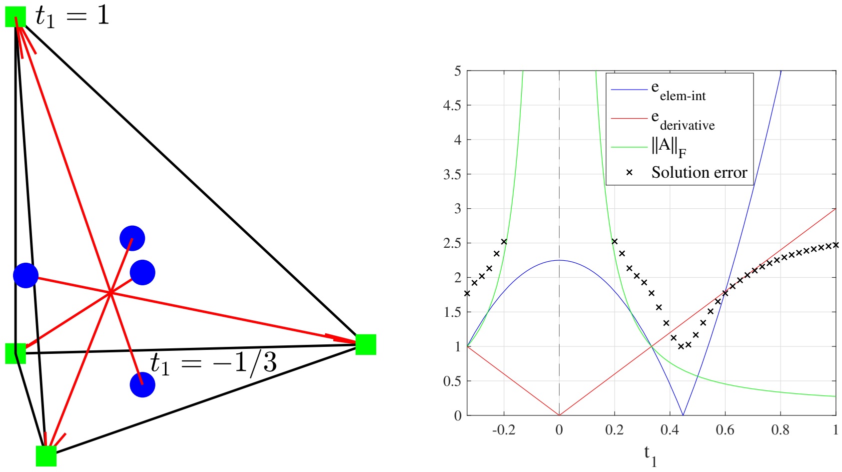

(c) Nodal locations for the reference tetrahedral element (d) Normalized solution error and objective functions using tetrahedral elements

Fig. 7. Nodal locations and solution error for $p = 1$ triangular and tetrahedral element operators with one $\mathrm{s}_{\text{c-vert}}$ symmetry group for the linear convection problem.

8 shows the solution error for the linear convection test case for the two- and three-dimensional operators with 50 different values of t_1 and w_1 for a total of 2500 test cases.

Once again, the solution error is minimized when the degree of the cubature rule is increased to $2p = 2$, which is the solution shown by the red line in Fig. 8. Since increasing the degree of the cubature rule significantly reduces the solution error, all of the free parameters in the cubature rules of SBP operators are subsequently used to increase the cubature rule's degree. The white space in the plots indicates operators that are not stable for the size of the time step used. These white areas coincide with the areas in Figs. 8b and 8d that have a higher value for the Frobenius norm of A for the triangular and tetrahedral operators, respectively. This once again indicates that the Frobenius norm of A is a good indicator of the spectral radius of the global operator matrix.

5.4. *Optimizing free parameters in* R_1

To investigate the impact of the free parameter in R_1, the operator given in Eq. (43) will be used but with $w_1 = 1/(12t_1^2)$, which sets the degree of the cubature rule to $2p = 2$. The two-dimensional results from the operators constructed with varying values of t_1 and r_1 are shown in Fig. 9. The dissipation of the energy, which is shown in Fig. 9b, matches the contour for the solution error in Fig. 9a. The matrix R_1 is used to interpolate/extrapolate the solution to the facet nodes, which is needed to apply the SATs. Since upwind SATs are used, which provide some dis-

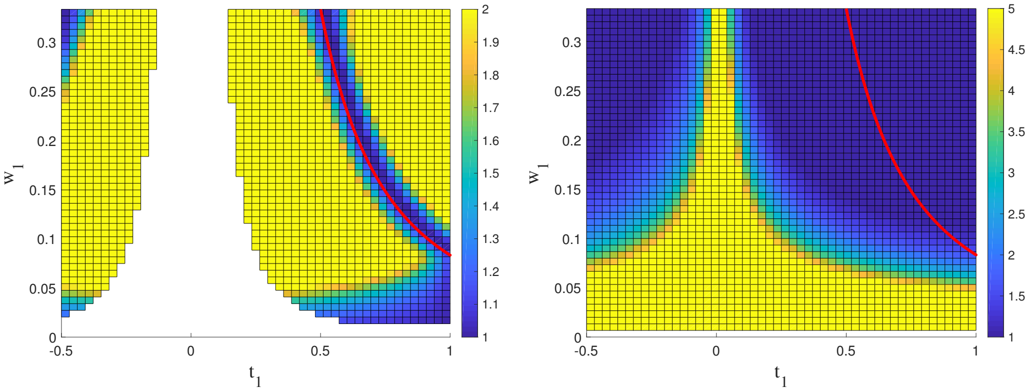

(a) Normalized solution error for triangular elements

(b) Frobenius norm of A for triangular elements

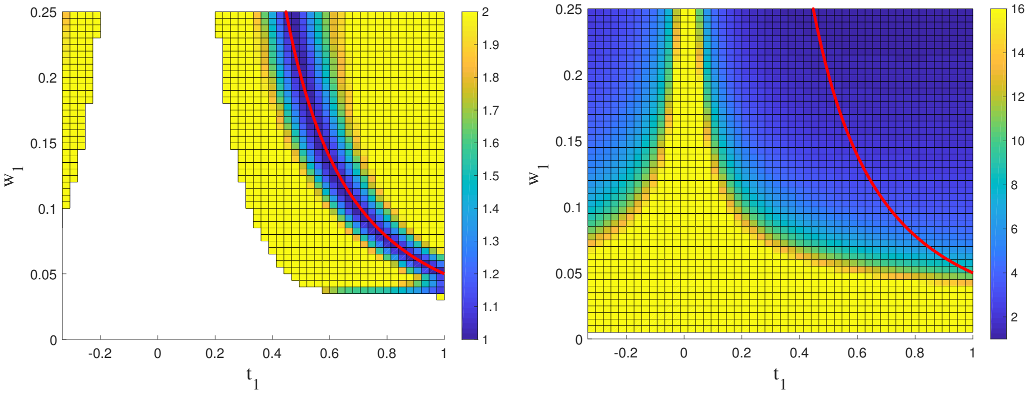

(c) Normalized solution error for tetrahedral elements

(d) Frobenius norm of A for tetrahedral elements

Fig. 8. Solution error for the linear convection problem and Frobenius norm of A for $p = 1$ triangular and tetrahedral element operators with the s_{cent} and one $s_{\text{c-vert}}$ symmetry group with $r_1 = 0$ from Eq. (43); the red line indicates a cubature rule of degree two.

sipation, it is logical to see that the free parameters in R_1 have an impact on the amount of dissipation being produced. The free parameters in R_1 can therefore be used to influence the amount of dissipation being produced.

Figs. 9c and 9d show the Frobenius norms of D_ξ and A, respectively. Comparing both of these figures to Fig. 9a it is clear that the contours of the Frobenius norm of A match more closely the area for which the operators are stable, particularly on the left edge of the plots where the weight on the $s_{\text{c-vert}}$ nodes is zero. The matrix A contains the term $\mathsf{H}^{-1}\mathsf{R}_1^T\mathsf{B}\mathsf{R}_1$ to approximate the contributions of the SATs to the global SBP operator. For a diagonal norm matrix in the form $\mathsf{H} = \text{diag}(h_1, h_2, \ldots, h_n)$, its inverse is $\mathsf{H}^{-1} = \text{diag}(1/h_1, 1/h_2, \ldots, 1/h_n)$. Consequently, when the weight on one or several nodes are very small, entries in H^{-1} become very large, thus increasing the Frobenius norm of A.

The red lines in the sub-figures of Fig. 9 show for the range of t_1 considered, $r_1 = 1/4$ when R_1 is calculated using the Moore-Penrose pseudoinverse. The red line on Fig. 9d is near the minimum Frobenius norm of A for all values of t_1. Furthermore, the red line in Fig. 9a is also outside of the area where the solution error is maximized for most values of t_1. Therefore, the use of the Moore-Penrose pseudoinverse to calculate R_1 provides a good compromise between minimizing the Frobenius norm of A, and thus the spectral radius, and returning an operator that minimizes the solution error. The results for the tetrahedral operator with the s_{cent} and one $s_{\text{c-vert}}$ symmetry group are analogous.

The results for the tetrahedral operator with the symmetry groups $s_{\text{c-vert}}$ and s_{cent} and with $p_{\text{cub}} = 2p = 2$ are shown in Fig. 10 and are nearly identical to the results in Fig. 9. The Moore-Penrose pseudoinverse solution once again provides an operator with a nearly minimized Frobenius norm of A and a low solution error for most of the range of t_1 considered. Therefore, in all future operators that are created, R_1 is calculated using the modified Moore-Penrose pseudoinverse equations in Appendix C. These modified equations ensure that R_1 is created such that it has symmetrical contributions across all symmetry lines and planes.

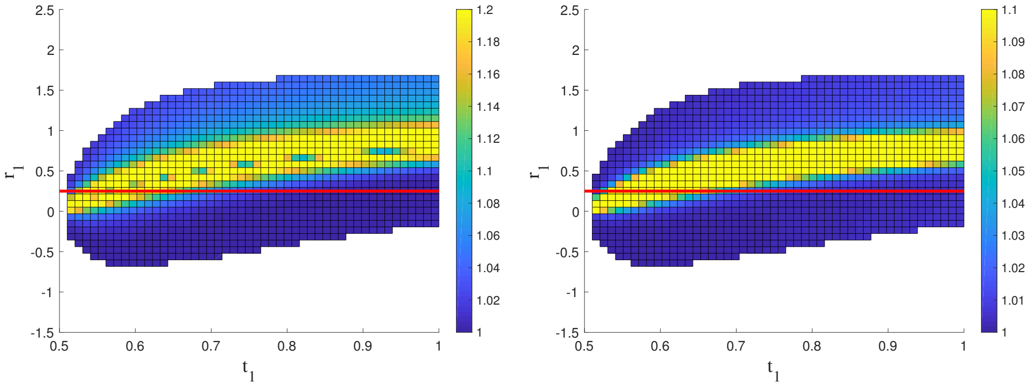

(a) Normalized solution error

(b) Normalized energy dissipation

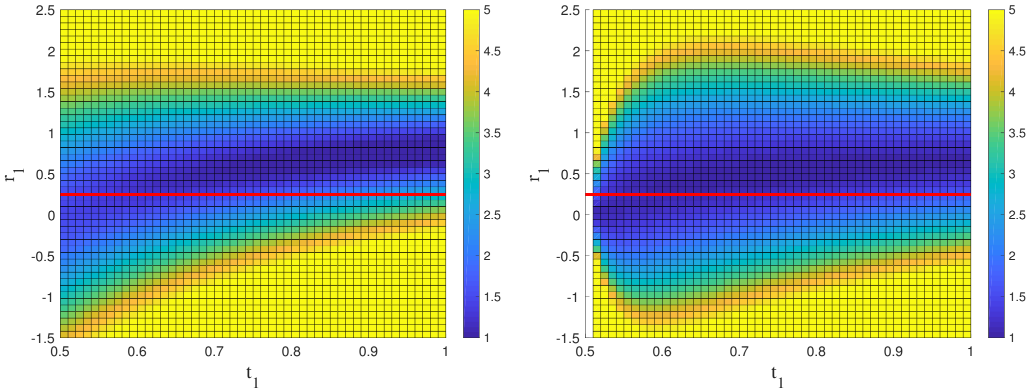

(c) Normalized Frobenius norm of D_ξ

(d) Normalized Frobenius norm of A

Fig. 9. Results for the $p = 1$ triangular operator with four element nodes (the s_{cent} and one $s_{\text{c-vert}}$ symmetry groups) and $p_{\text{cub}} = 2$, where the red line indicates the value of r_1 found using the Moore-Penrose pseudoinverse to calculate R_1.

5.5. *Optimizing free parameters in* S_ξ

From Section 4.3 it was shown that an operator must have at least $N^*_{p,d} + 2$ element nodes for there to be any free parameters in S_ξ. The simplest triangular operator that has at least one free parameter in S_ξ is the $p = 1$ R^0 operator with the LG facet quadrature rule, which has six element nodes. There are no free parameters in either the cubature rule or in R_1 since all of the element nodes are collocated with facet nodes. There are three free parameters in S_ξ, one of which is set to zero in order to be able to vary the other two and plot the results on a two-dimensional surface plot. The normalized solution error along with two objective functions are shown in Fig. 11. The solution error in Fig. 11a indicates that the free parameters in S_ξ have very little impact on the solution error, but they have a significant impact on the CFL number that can be used. When the CFL number is increased from 0.01 in Fig. 11a to 0.1 in Fig. 11b, the combination of values for s_1 and s_2 that give a stable operator for the time marching method used is significantly reduced. The small area of stability when CFL = 0.1 matches with the minimum of the Frobenius norm of A in Fig. 11c. Additionally, the combination of s_1 and s_2 that minimizes $e_{\text{derivative}}$, which is shown in Fig. 11d, matches the area where the Frobenius norm of A is also minimized. Therefore, if the free parameters in S_ξ are used to minimize the Frobenius norm of A, the operator will have a small spectral radius and a small truncation error as well.

There is a clear benefit to minimizing the Frobenius norm of A and this optimization problem is discussed in Theorem 4, which is stated next.

Theorem 4. *The minimization problem to satisfy the accuracy conditions* $\mathsf{D}_\xi \boldsymbol{p}_k = \boldsymbol{p}'_k$, $\forall k \in \{1, 2, \dots, N^*_{p,d}\}$ *and to minimize the Frobenius norm of* $\mathsf{A} = \mathsf{D}_\xi + \mathsf{H}^{-1} R_1^T \mathsf{B} \mathsf{R}_1$ *is a convex optimization problem.*

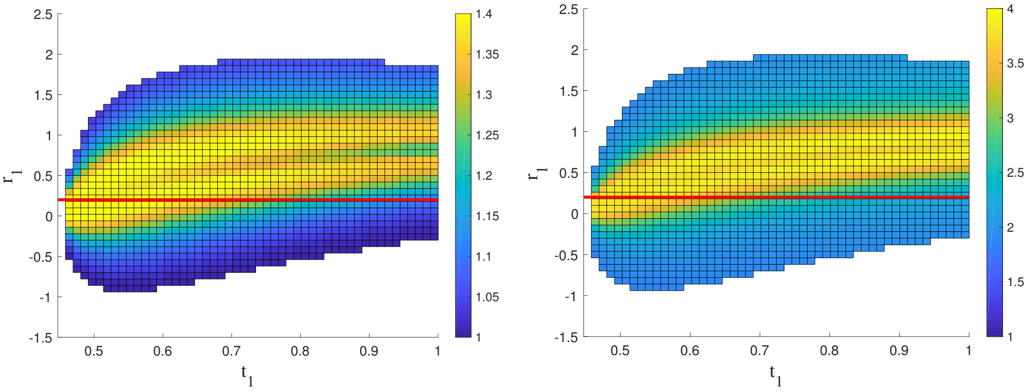

(a) Normalized solution error (b) Normalized energy dissipation

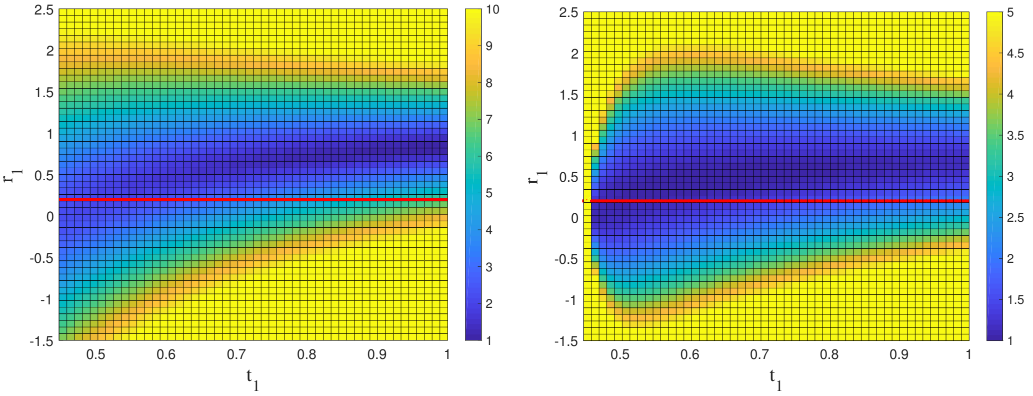

(c) Normalized Frobenius norm of D_ξ (d) Normalized Frobenius norm of A

Fig. 10. Results for the $p = 1$ tetrahedral operator with five element nodes ($\mathrm{s}_{\mathrm{cent}}$ and one $\mathrm{s}_{\text{c-vert}}$ symmetry groups) and $p_{\mathrm{cub}} = 2$, where the red line indicates the value of r_1 found using the Moore-Penrose pseudoinverse to calculate R_1.

Proof: The linear constrains are presented in Appendix D. The matrix A is recast in the form

$$\begin{aligned}\mathsf{A} &= \mathsf{D}_\xi + \mathsf{H}^{-1} R_1^T \mathsf{B} \mathsf{R}_1 \\ &= \mathsf{H}^{-1}\mathsf{Q}_\xi + \mathsf{H}^{-1} R_1^T \mathsf{B}\mathsf{R}_1 \\ &= \mathsf{H}^{-1}\left(\mathsf{S}_\xi + \underbrace{\frac{1}{2}\mathsf{E}_\xi + R_1^T \mathsf{B}\mathsf{R}_1}_{\mathsf{G}}\right),\end{aligned} \tag{44}$$

where G is a symmetric matrix. To help identify the components of the matrix A, consider an operator with three element nodes

$$\begin{aligned}\mathsf{A} &= \mathsf{H}^{-1}(\mathsf{S}_\xi + \mathsf{G}) \\ &= \begin{bmatrix} 1/h_1 & 0 & 0 \\ 0 & 1/h_2 & 0 \\ 0 & 0 & 1/h_3 \end{bmatrix} \left(\begin{bmatrix} 0 & s_{1,2} & s_{1,3} \\ -s_{1,2} & 0 & s_{2,3} \\ -s_{1,3} & -s_{2,3} & 0 \end{bmatrix} + \begin{bmatrix} g_{1,1} & g_{1,2} & g_{1,3} \\ g_{1,2} & g_{2,2} & g_{2,3} \\ g_{1,3} & g_{2,3} & g_{3,3} \end{bmatrix} \right) \\ &= \begin{bmatrix} g_{1,1}/h_1 & (g_{1,2}+s_{1,2})/h_2 & (g_{1,3}+s_{1,3})/h_3 \\ (g_{1,2}-s_{1,2})/h_1 & g_{2,2}/h_2 & (g_{2,3}+s_{2,3})/h_3 \\ (g_{1,3}-s_{1,3})/h_1 & (g_{2,3}-s_{2,3})h_2 & g_{3,3}/h_3 \end{bmatrix}.\end{aligned} \tag{45}$$

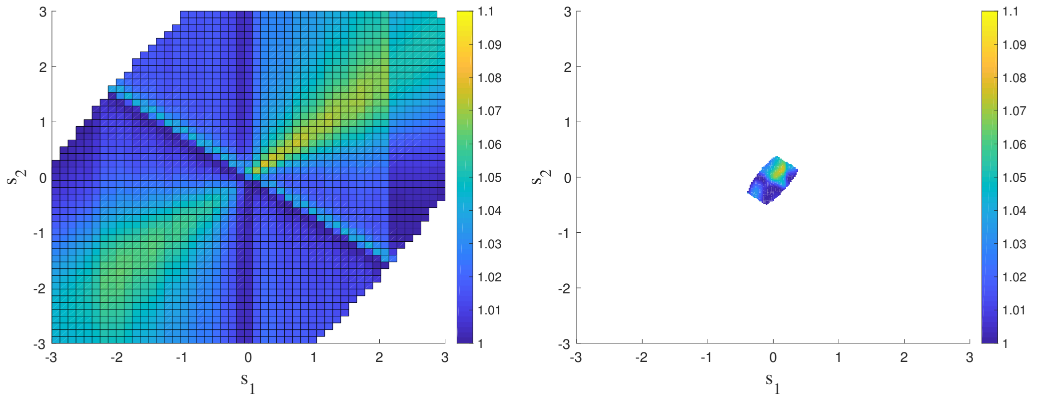

(a) Normalized solution error with CFL= 0.01

(b) Normalized solution error with CFL= 0.1

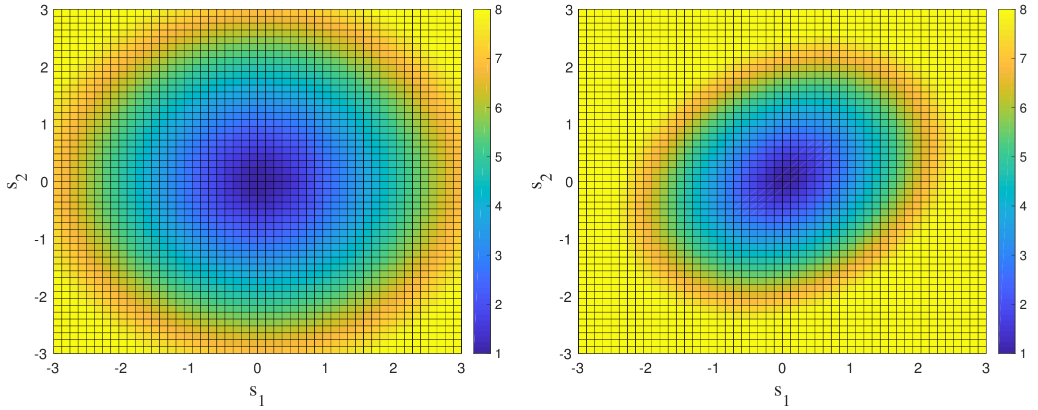

(c) Normalized Frobenius norm of A

(d) Normalized $e_{\text{derivative}}$

Fig. 11. Normalized solution error for the linear convection problem and objective functions for the $p = 1$ triangular diagonal-E operator with $p_{\text{cub}} = 1$ and $n = 6$.

For a matrix A of arbitrary size its entries are

$$A_{i,j} = \begin{cases} (g_{i,j} + s_{i,j})/h_i & i < j, \\ g_{i,j}/h_i & i = j, \\ (g_{i,j} - s_{i,j})/h_i & i > j. \end{cases} \tag{46}$$

Eq. (24) indicates that the Frobenius norm of a matrix is simply the square of all of its entries. Therefore, the objective function J for the minimization of the Frobenius norm of A is simply

$$J = \sum_{i=1}^{n-1} \sum_{j=i+1}^{n} \left(\frac{g_{i,j} + s_{i,j}}{h_i} \right)^2 + \sum_{j=1}^{n-1} \sum_{i=j+1}^{n} \left(\frac{g_{i,j} - s_{i,j}}{h_i} \right)^2 + \sum_{i=1}^{n} \left(\frac{g_{i,i}}{h_i} \right)^2 . \tag{47}$$

To find the gradient of J, the single index notation $k = (j-2)(j-1)/2 + i, i < j$ is used. The case when $i = j$ does not need to be considered since these terms do not appear in the gradient of J. The gradient of J with respect to the entries in S_ξ is

$$\frac{\partial J}{\partial s_k} = 2 \left(\frac{g_k + s_k}{h_i} - \frac{g_k - s_k}{h_j} \right), \tag{48}$$

and the Hessian of J is

$$\frac{\partial^2 J}{\partial s_k^2} = 2 \left(\frac{1}{h_i} + \frac{1}{h_j} \right). \tag{49}$$

Since all the diagonal entries in H are positive, all of the entries in the Hessian of J are also positive and thus, the optimization problem is convex with linear constraints. This completes the proof. The same analysis can also be used to show that the minimization of the Frobenius norm of the matrix D_ξ is also convex.

5.6. Summary

Based on the results of this section, the following methodology can be followed to construct optimized SBP operators:

1. Construct a cubature rule of degree $2p - 1$ and with positive weights
    - Use any free parameters to get $p_{\text{cub}} = 2p$
2. Use the equations in Appendix C to construct R_1 and the equations in Appendix A.3 to permute R_1 to all of the other facets
3. Construct E_ξ using Eq. (5)
4. Construct S_ξ with the convex optimization method from Section 5.5 to minimize the Frobenius norm of A
5. Use the properties from Definition 1 to construct Q_ξ and D_ξ
6. Permute all of the directional operators using Eq. (9)

There may be free parameters in the cubature rule remaining even after the degree of the cubature rule is increased from $2p - 1$ to $2p$. In the optimization of triangular and tetrahedral operators in Sections 6 and 7, respectively, any remaining free parameters are used to obtain cubature rules of degree $2p + 1$. Therefore, there are no free parameters in the cubature rule after step 1 in the optimization procedure given above.

In the paper by Friedrich *et al.* [29], degree preserving SBP operators on non-conforming meshes were investigated. It was shown that degree preserving operators could be constructed when the degree of the cubature rule is $2p$ or greater. Therefore, increasing the degree of the cubature rule from $2p - 1$ to $2p$ or higher is beneficial to reduce the solution error and also to have degree preserving SBP operators on non-conforming meshes.

6. Optimized operators on triangular elements

Section 5 determined how the free parameters in the cubature rule, R_1 and S_ξ should be used to optimize the SBP operators. However, the cost benefit trade-off between the additional computational cost of having extra element nodes versus the further optimization that can be done with the extra DOF was not considered. This section investigates this cost benefit trade-off by comparing operators with different cubature rules with $p_{\text{cub}} = 2p - 1$ to $p_{\text{cub}} = 2p + 1$ for the SBP R^d, R^{d-1} and R^0 families. All of the free parameters in the cubature rule, R_1 and S_ξ are optimized according to the results from Section 5. To compare the computational cost of the different operators, the CPU time is calculated by multiplying the number of processors by the run time [2]. Each operator is run on the same set of meshes that get progressively finer. Some operators that are derived have the same cubature rule as previously derived SBP operators, and when $n = N^*_{p,d}$, the SBP operators are identical since there are no free parameters.

To compare the solution error of different operators it is important that they have the same computational cost. Since operators with different number of element nodes are compared, the solution error needs to be interpolated to a common computational cost in order to allow the results to be compared. The common computational cost is selected as the least expensive run on the finest mesh. The difference in the solution error between an operator and a reference operator is calculated as

$$e_{\text{s,diff}} = \frac{e_{\text{s}} - e_{\text{s,ref}}}{e_{\text{s,ref}}} \times 100, \tag{50}$$

where $e_{\text{s,ref}}$ is the solution error of the reference operator at the common computational cost and e_{s} is the solution error of the operator being compared also at the common computational cost. To also compare the number of element nodes for an operator to a reference operator we use

$$\Delta n\% = \frac{n - n_{\text{ref}}}{n_{\text{ref}}} \times 100, \tag{51}$$

---

[2] The code that is utilized is optimized for flexibility rather than speed. Only the relative CPU time of the different operators is of interest.

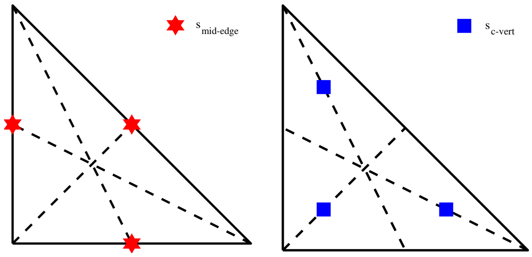

(a) Cubature rule #1 (b) Cubature rule #2

Fig. 12. Two cubature rules with $n = 3$ and $p_{\text{cub}} = 2$.

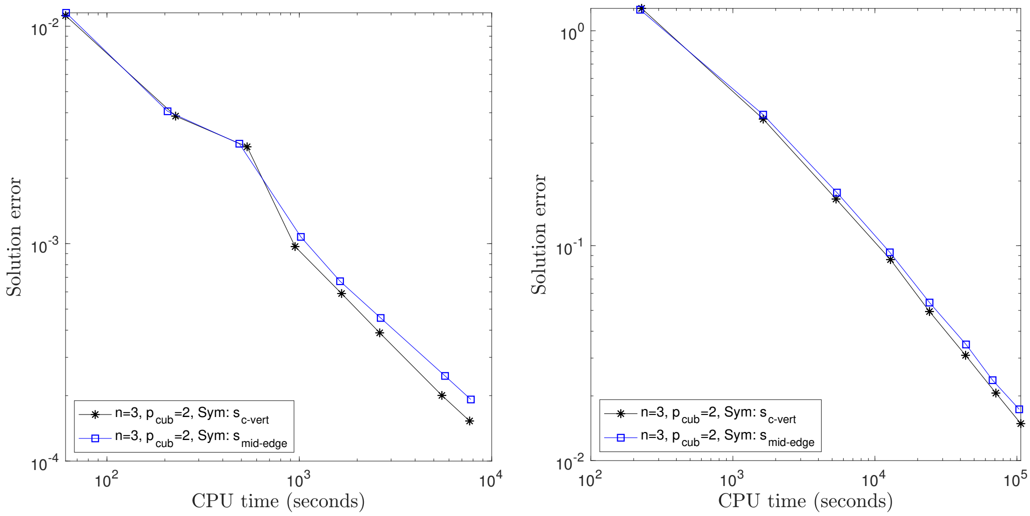

(a) Periodic linear convection test case (b) Isentropic vortex test case

Fig. 13. Solution error and computational cost for $p = 1$ R^d operators on triangular elements.

where n_{ref} is the number of element nodes for the reference operator. The reference operator is selected as the operator with a previously used cubature rule with the fewest element nodes. The reference operator used for each case is clearly identified.

6.1. R^d *operators*

The operators in the R^d family do not have any restrictions in terms of nodal locations, but they require $n \geq N^*_{p,d}$ and $p_{\text{cub}} \geq 2p - 1$.

6.1.1. $p = 1$ R^d *operators*

Two operators in the R^d family with $n = N^*_{1,2} = 3$ and $p_{\text{cub}} = 2p = 2$ are derived and shown in Fig. 12. The operator in Fig. 12b has the same cubature rule and is identical to an operator previously derived in [7]. Table 3 indicates that to have an R^d operator with $p_{\text{cub}} = 2p+1 = 3$ three DOF are required. The combination of the symmetry groups $\text{s}_{\text{c-vert}}$ and s_{cent} provides three DOF but the cubature rule that is created contains a negative weight, which is not permitted for an SBP operator with a diagonal norm matrix. It is possible to create an operator with $p_{\text{cub}} = 3$ and positive weights with two $\text{s}_{\text{c-vert}}$ symmetry groups but this combination of symmetry groups has a sufficient number of element nodes for a $p = 2$ operator, which is considered in the next subsection. The results for both test cases for the $p = 1$ R^d operators are shown in Fig. 13. Since both operators have the same number of element nodes, they have the same computational cost for each mesh. However, the operator in Fig. 12b has a slightly lower solution error for both test cases. Hence, the operator in Fig. 12b is the slightly more efficient $p = 1$ R^d operator.

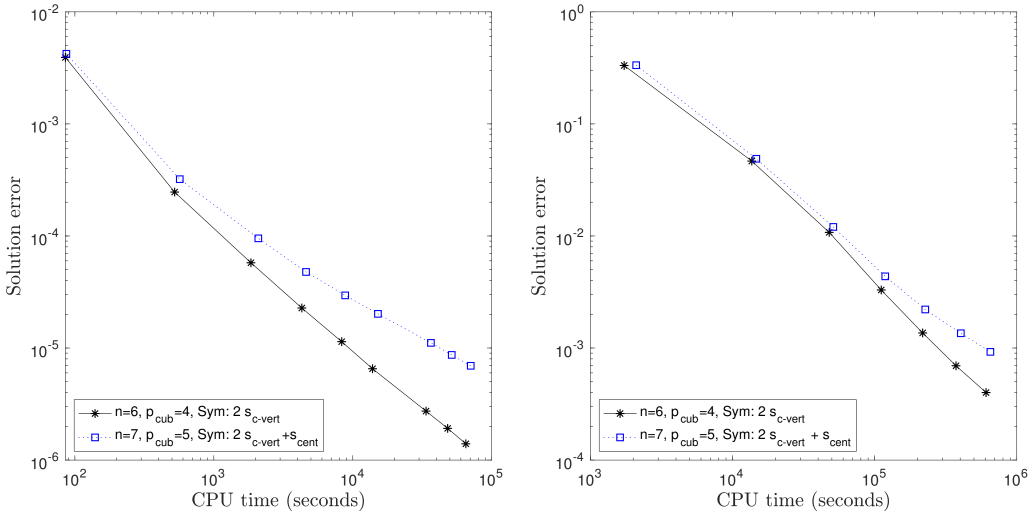

(a) Periodic linear convection test case (b) Isentropic vortex test case

Fig. 14. Solution error and computational cost for $p = 2$ R^d operators on triangular elements.

Table 4: Properties of symmetry groups on a triangle with element nodes on the facets.

Element symmetry groups	n	n_f	n/n_f	DOF	n/DOF
$\mathrm{s}_{\mathrm{vert}}$	3	2	3/2	1	3
$\mathrm{s}_{\mathrm{edge}}$	6	2	3	2	3
$\mathrm{s}_{\mathrm{mid\text{-}edge}}$	3	1	3	1	3

6.1.2. $p = 2$ R^d *operators*

A $p = 2$ operator with $n = N^*_{2,2} = 6$ and $p_{\mathrm{cub}} = 2p = 4$ is derived along with another operator with $n = 7$ and $p_{\mathrm{cub}} = 2p + 1 = 5$ in the R^d family. Fig. 14 shows the results for both test cases for these operators. For both test cases and on all meshes, the operator with $n = 6$ has a lower computational cost, since it has fewer element nodes, and it also has a lower solution error. Therefore, the operator with $n = 6$, which has the same cubature rule and is identical to an operator previously derived in [7], is the preferred $p = 2$ R^d operator.

6.2. R^{d-1} *operators*

In order for the interpolation/extrapolation of operators in the two-dimensional R^{d-1} family to span only $d - 1$ dimensions, they require at least $N^*_{p,2-1} = p + 1$ element nodes on each of the facets. In order to minimize the number of element nodes in the operator it is helpful for the element nodes that are on the facets to be on several facets. For example, element nodes for triangular operators that are at the vertices are on two facets. Therefore, if each facet requires two nodes, only three element nodes are required by placing them at the vertices. Alternatively, if the element nodes are not placed at the vertices, a total of six element nodes are required instead. Another important consideration when selecting which symmetry groups to have on the facets is the ratio of element nodes to DOF. As Table 4 indicates, the ratio n/DOF is the same for each of the symmetry groups on a triangle. However, as will be shown in Section 7.2, this is not the case for three-dimensional operators.

6.2.1. $p = 1$ R^{d-1} *operators*

A $p = 1$ R^{d-1} operator requires at least $p + 1 = 2$ element nodes on each of the facets. Table 4 indicates that the symmetry groups $\mathrm{s}_{\mathrm{vert}}$ and $\mathrm{s}_{\mathrm{edge}}$ both have two element nodes on each of the facets. Fig. 15 shows the numerical errors for the constructed $p = 1$ R^{d-1} operators. The operator with $n = 3$ has the same cubature rule and is identical to a previously derived operator in [6]. The operators with $p_{\mathrm{cub}} > 2p - 1$ have a solution error that is significantly lower than the operator with $p_{\mathrm{cub}} = 2p - 1 = 1$. The exception to this is the operator with $n = 6$, which performed well for the linear convection test case but poorly for the Euler test case. The operator with $n = 4$, which is the most efficient

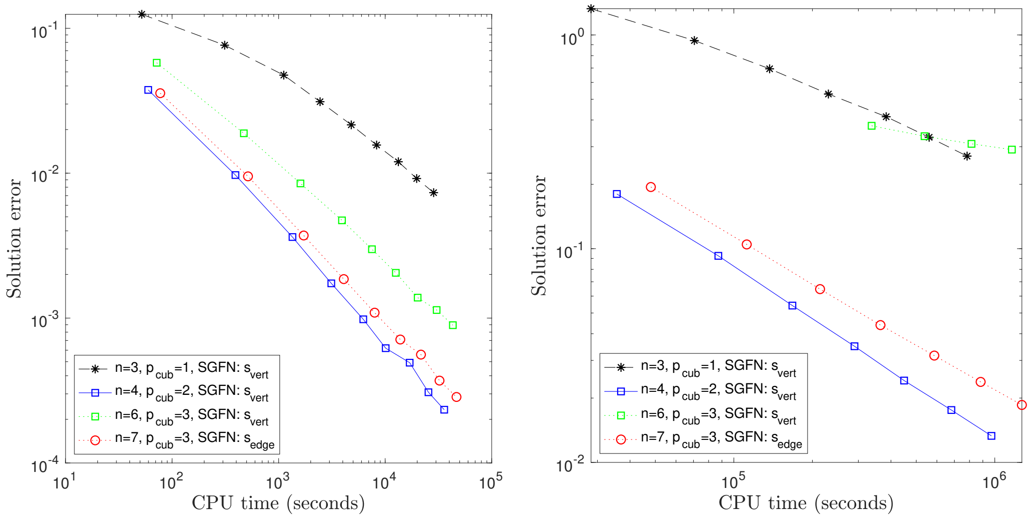

(a) Periodic linear convection test case

(b) Isentropic vortex test case

Fig. 15. Solution error and computational cost for $p = 1$ R^{d-1} operators on triangular elements, where SGFN stands for symmetry groups with facet nodes.

Table 5: Comparison of LG and LGL facet quadrature rules for triangular elements where $n_{\text{sym}} = [n_{s_{\text{cent}}}, n_{s_{\text{c-vert}}}, n_{s_{\text{vert}}}]$, and n is the number of element nodes for the triangular element.

p	Quad rule	Facet quad degree	n_{sym}	n_f	n	DOF	n/DOF
even	LG	$2p+1$	$[1, \frac{p}{2}, 0]$	$p+1$	$3(p+1)$	$\frac{p+2}{2}$	$\frac{6(p+1)}{p+2}$
	LGL	$2p+1$	$[0, \frac{p}{2}, 1]$	$p+2$	$3(p+1)$	$\frac{p+2}{2}$	$\frac{6(p+1)}{p+2}$
odd	LG	$2p+1$	$[1, \frac{p+1}{2}, 0]$	$p+1$	$3(p+1)$	$\frac{p+1}{2}$	6
	LGL	$2p+1$	$[1, \frac{p-1}{2}, 1]$	$p+2$	$3(p+1)$	$\frac{p+1}{2}$	6

for both test cases, has a reduction in the solution error of $e_{\text{s,diff}} = -96\%$ and $e_{\text{s,diff}} = -94\%$ for the linear convection and isentropic vortex test cases, respectively, compared to the previously published $n = 3$ operator.

6.2.2. $p = 2$ R^{d-1} *operators*

The $p = 2$ R^{d-1} operators must have at least $p + 1 = 3$ element nodes on each of the facets. Since this is an odd number of nodes, the symmetry group $\mathsf{s}_{\text{c-edge}}$ must be used along with either s_{vert} or s_{edge}. Fig. 16 shows the numerical error for the operators constructed with both of these symmetry groups that have facet nodes. Unlike the previous operators considered, the operator with the lowest solution error is not the same for both test cases. The operator with $n = 9$ and $p_{\text{cub}} = 2p = 4$ has the lowest solution error for the linear convection test case, while the operator with $n = 12$ and $p_{\text{cub}} = 2p + 1 = 5$ has the lowest solution error for the isentropic vortex test case. When both test cases are considered, the operator with $n = 12$ is preferable since it has the second lowest solution error for the linear convection test case and the lowest solution error for the isentropic vortex test case. The reduction in the solution error for the operator with $n = 12$ compared to the $n = 7$ operator is $e_{\text{s,diff}} = -52\%$ and $e_{\text{s,diff}} = -39\%$ for the linear convection and isentropic vortex test cases, respectively.

6.3. R^0 *operators*

The R^0 operators are assembled by first constructing a facet cubature rule with $p_{\text{cub}} \geq 2p$. For triangular operators, the facets are simply lines and the LG and LGL quadrature rules are used. Table 5 indicates that while the LG quadrature rule has one fewer node per facet than the LGL facet quadrature rule, they both contribute the same number of element nodes since the LGL quadrature rule has element nodes on the vertices, which are thus on two facets. Both quadrature rules also have the same ratio n/DOF.

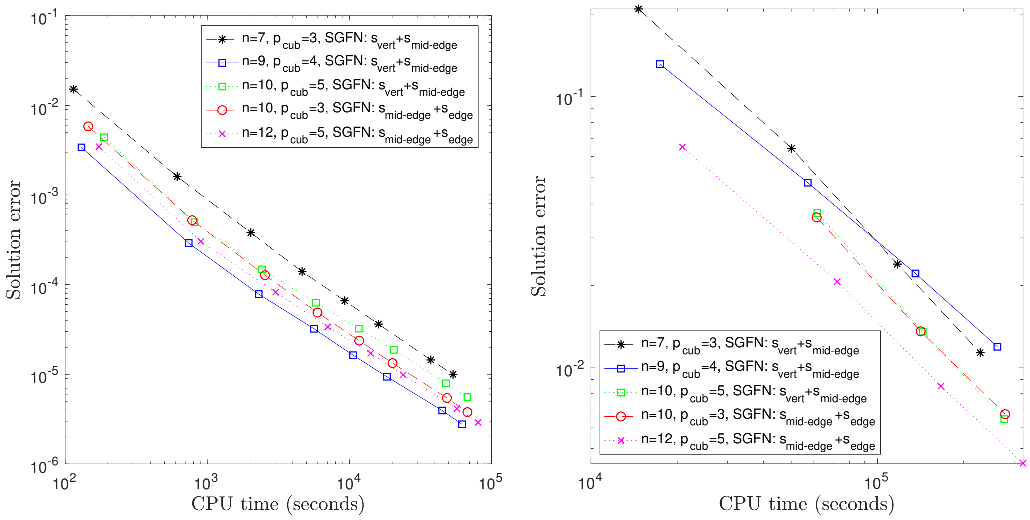

(a) Periodic linear convection test case (b) Isentropic vortex test case

Fig. 16. Solution error and computational cost for $p = 2$ R^{d-1} operators on triangular elements, where SGFN stands for symmetry groups with facet nodes.

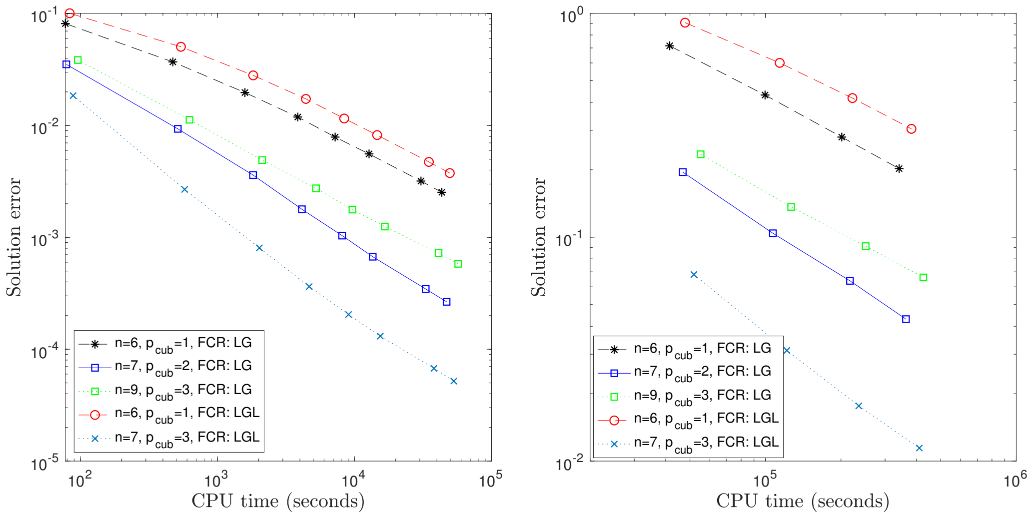

(a) Periodic linear convection test case (b) Isentropic vortex test case

Fig. 17. Solution error and computational cost for $p = 1$ R^0 operators on triangular elements, where FCR stands for facet cubature rule.

6.3.1. $p = 1$ R^0 *operators*

The numerical results for the $p = 1$ R^0 family are shown in Fig. 17. The operator with $n = 6$ and the LG facet quadrature rule and the operator with $n = 7$ and the LGL facet quadrature have the same cubature rules as operators previously derived in [24] and [30], respectively. The operator with the lowest solution error for both test cases is the one with $n = 7$ and the LGL facet quadrature rule. This operator has $e_{\mathrm{s,diff}} = -97\%$ and $e_{\mathrm{s,diff}} = -93\%$ for the linear convection and isentropic vortex test cases, respectively, compared to the $n = 6$ LG facet quadrature rule operator.

6.3.2. $p = 2$ R^0 *operators*

Fig. 18 shows the solution error for the constructed $p = 2$ R^0 operators. The operator with $n = 10$ and the LG facet quadrature rule as well as the one with $n = 12$ and the LGL facet quadrature rule have the same cubature rule as previously constructed operators in [24] and [30], respectively. The operator with $n = 12$ and the LGL facet quadrature rule has the lowest solution error for both test cases and has $e_{\mathrm{s,diff}} = -79\%$ and $e_{\mathrm{s,diff}} = -80\%$ for the

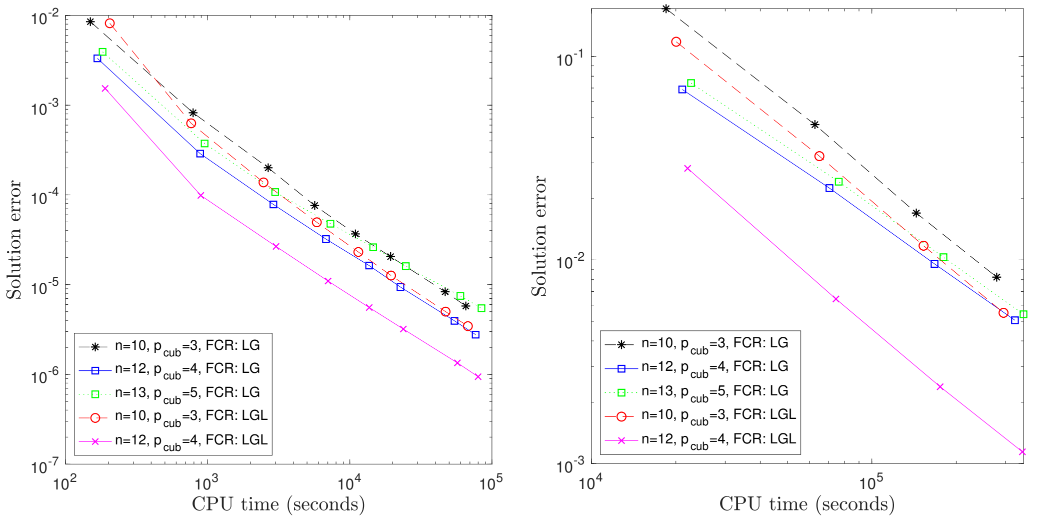

(a) Periodic linear convection test case

(b) Isentropic vortex test case

Fig. 18. Solution error and computational cost for $p = 2$ R^0 operators on triangular elements, where FCR stands for facet cubature rule.

Table 6: Summary of results for the triangular operators, where LCE stand for linear convection equation, FCR is facet cubature rule, and where novel cub. refers to novel cubature rules used for SBP operators.

Family	p	ID	p_{cub}	$e_{\text{s,diff}}$		Diff. in n		Novel cub.
				LCE	Euler eq.	Δn	$\Delta n\%$	
R^d	1	$n = 3$	$2p = 2$	-	-	-	-	✗ [7]
	2	$n = 6$	$2p = 4$	-	-	-	-	✗ [7]
R^{d-1}	1	$n = 3$	$2p - 1 = 1$	-	-	-	-	✗ [6]
		$n = 4$	$2p = 2$	-96%	-94%	1	33%	✓
	2	$n = 7$	$2p - 1 = 3$	-	-	-	-	✗ [6]
		$n = 9$	$2p = 4$	-66%	29%	2	29%	✓
		$n = 12$	$2p + 1 = 5$	-52%	-39%	5	71%	✓
R^0	1	$n = 6$ FCR: LG	$2p - 1 = 1$	-	-	-	-	✗ [24]
		$n = 7$, FCR: LGL	$2p + 1 = 3$	-97%	-93%	1	17%	✗ [30]
	2	$n = 10$ FCR: LG	$2p - 1 = 3$	-	-	-	-	✗ [24]
		$n = 10$ FCR: LGL	$2p - 1 = 3$	-37%	-24%	0	0%	✓
		$n = 12$, FCR: LGL	$2p = 4$	-79%	-80%	2	20%	✗ [30]

linear convection and isentropic vortex test cases, respectively, compared to the $n = 10$ operator with the LG facet quadrature rule.

6.3.3. Summary of results

Table 6 provides a summary of the derived triangular operators with an indication of the reduction in solution error as well as the number of element nodes compared to reference operators. In the comparison of the two-dimensional operators, there is a clear benefit to increasing the degree of the cubature rule beyond $2p - 1$. The operators with $p_{\text{cub}} = 2p$ are generally the most efficient but there are a few exceptions. The operator that was found to be the most efficient for the $p = 2$ R^{d-1} family has $p_{\text{cub}} = 2p + 1$. However, no operator with the same facet symmetry groups with $p_{\text{cub}} = 2p$ was derived. Similarly, the most efficient $p = 1$ R^0 operator has $p_{\text{cub}} = 2p + 1 = 3$, but there is no operator that was derived with $p_{\text{cub}} = 2p$ with the same facet quadrature rule. Thus, it appears that there is only a benefit of increasing the degree of the cubature rule to $2p + 1$ when an operator with $p_{\text{cub}} = 2p$ cannot be derived with the same facet symmetry groups. In all but one case, the operator with the lowest solution error for a given

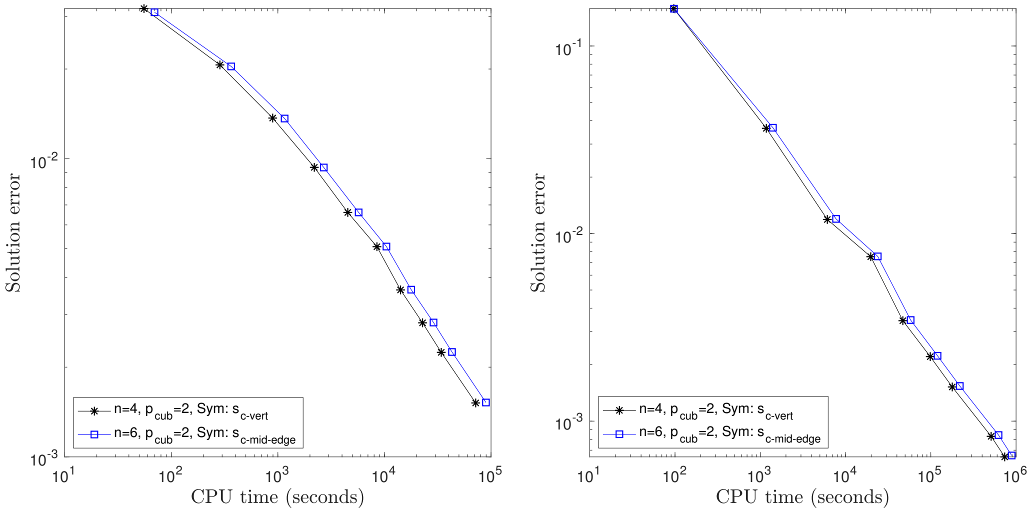

(a) Periodic linear convection test case

(b) Manufactured Euler solution test case

Fig. 19. Solution error and computational cost for $p = 1$ R^d operators on tetrahedral elements.

computational cost for one test case was also the best operator for the other test case as well. This is a good indication that the operators that are found to be efficient for these two test cases are efficient for a large variety of test cases with smooth solutions.

7. Optimized operators on tetrahedral elements

This section investigates different tetrahedral operators and it is formatted in the same way as Section 6. Once again, the free parameters in the operators are optimized according to the results from Section 5.

7.1. R^d *operators*

The R^d operators require $n \geq N_{p,3} = (p+1)(p+2)(p+3)/6$ element nodes and $p_{\text{cub}} \geq 2p-1$.

7.1.1. $p = 1$ R^d *operators*

The $p = 1$ R^d operators require at least $n = N^*_{1,3} = 4$ and $p_{\text{cub}} \geq 2p - 1 = 1$. Operators with the $\mathrm{s}_{\text{c-vert}}$ and $\mathrm{s}_{\text{c-mid-edge}}$ symmetry groups are both used to construct operators with $p_{\text{cub}} = 2p$. When the s_{cent} element node is used along with the previous two symmetry groups, the cubature rules that are found have negative weights; thus they cannot be used. The solution errors for both three-dimensional test cases for these operators are shown in Fig. 19. The operator with $n = 4$, which is identical to the operator previously derived in [30], has the lowest solution error in all cases, since it has fewer element nodes, and it also has a lower solution error as well.

7.1.2. $p = 2$ R^d *operators*

Operators with $p_{\text{cub}} = 2p-1, 2p$ and $2p+1$ are generated and their results are shown in Fig. 20. The operator with $n = 10$ is identical to the one derived in [30] and it has the lowest solution error for both test cases. This is the first comparison of the operators where an operator with $p_{\text{cub}} = 2p - 1$ has the lowest solution error. This deviation from the trend is likely due to the free parameters present in R_1. The R^0 operators never have any free parameters in R_1 and all of the generated R^{d-1} operators have exactly $\mathsf{N}^*_{p,d-1}$ element nodes on each of the facets, and thus they do not have any free parameters in R_1 either. Meanwhile, the R^d operators have free parameters in R_1 only when $n > N^*_{p,d}$. In all the previous cases for the R^d operators, in two and three dimensions, the most efficient operators have $p_{\text{cub}} = 2p$ and $n = N^*_{p,d}$, which means they do not have any free parameters in R_1. In this case however, the operator with $p_{\text{cub}} = 2p$ has $n > N^*_{p,d}$, and thus, has free parameters in R_1. As detailed in Section 5.4, the method used to optimize the free parameters in R_1 returns a solution with a low Frobenius norm of A but not necessarily the operator that provides the solution with the lowest error.

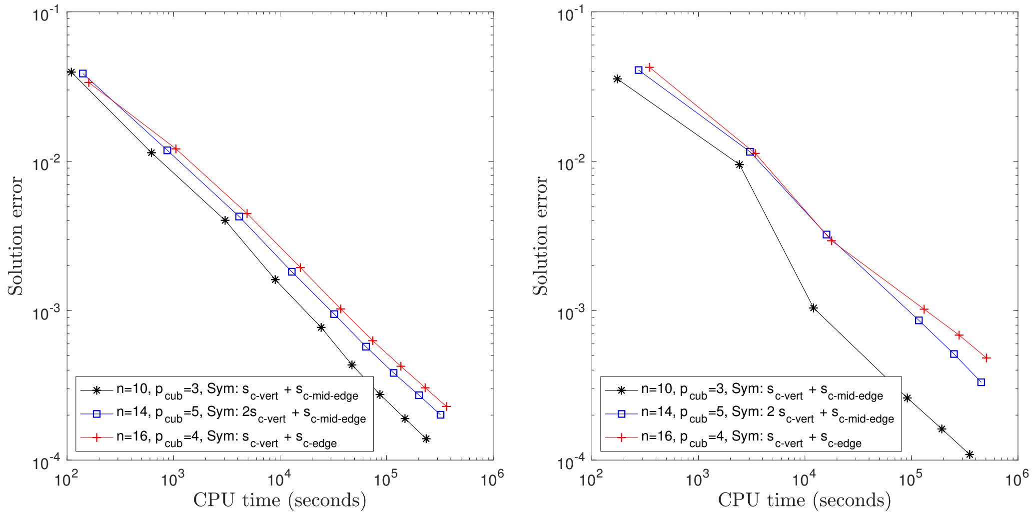

(a) Periodic linear convection test case

(b) Manufactured Euler solution test case

Fig. 20. Solution error and computational cost for $p = 2$ R^d operators on tetrahedral elements.

Table 7: Properties of symmetry groups on a tetrahedron with element nodes on the facets.

Element symmetry groups	n	n_f	n/n_f	DOF	n/DOF
s_{vert}	4	3	4/3	1	4
s_{edge}	12	6	2	2	6
$s_{\text{mid-edge}}$	6	3	2	1	6
$s_{\text{face-cent}}$	4	1	4	1	4
$s_{\text{c-face-vert}}$	12	3	4	2	6
s_{face}	24	6	4	3	8

7.2. R^{d-1} *operators*

As indicated in Section 6.2, the ratios n/n_f and n/DOF are both important for the R^{d-1} operators. Table 7 shows these two ratios for all of the symmetry groups that have element nodes on the facets. The symmetry group s_{vert} has the best properties for both of these important ratios.

7.2.1. $p = 1$ R^{d-1} *operators*

The $p = 1$ R^{d-1} operators require at least $N^*_{1,2} = 3$ element nodes on each of the facets, which can be provided by the symmetry group s_{vert}. Fig. 21 shows the solution error for the generated operators on both test cases. The operator with $n = 5$ and $p_{\text{cub}} = 2p = 2$ has the lowest solution error in both cases and $e_{\text{s,diff}} = -94\%$ and $e_{\text{s,diff}} = -96\%$ for the linear and Euler test cases, respectively, relative to the $n = 4$ operator.

7.2.2. $p = 2$ R^{d-1} *operators*

The $p = 2$ R^{d-1} operators require at least $N^*_{2,2} = 6$ element nodes on each of the facets. For all of the operators the symmetry group s_{vert} is used since it has the most desirable properties, as indicated by Table 7. For the next three nodes that are required, either the symmetry group $s_{\text{c-face-vert}}$ or $s_{\text{mid-edge}}$ can be used. The former symmetry group has a lower n/n_f ratio while the latter has a lower n/DOF ratio.

Operators are constructed with the combination of both of these symmetry groups, and their results are shown in Fig. 22. The operator with $n = 11$ has the same cubature rule as a previously published operator in [6]. The operator with $n = 20$, which has the lowest solution error for both test cases, has $e_{\text{s,diff}} = -73\%$ and $e_{\text{s,diff}} = -86\%$ for the linear convection and Euler test cases, respectively, compared to the $n = 11$ operator.

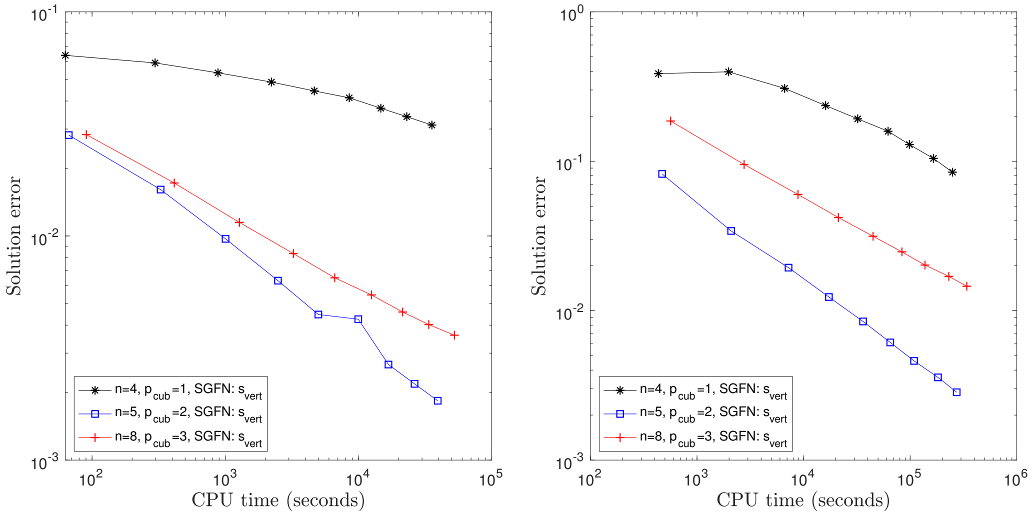

(a) Periodic linear convection test case

(b) Manufactured Euler solution test case

Fig. 21. Solution error and computational cost for $p = 1$ R^{d-1} operators on tetrahedral elements with CFL $= 0.02$, where SGFN stands for symmetry groups with facet nodes.

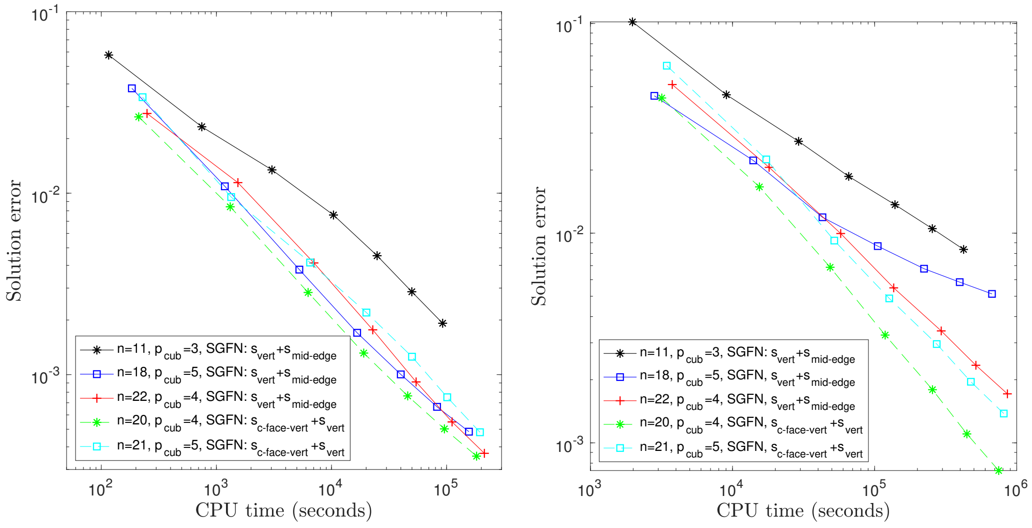

(a) Periodic linear convection test case

(b) Manufactured Euler solution test case

Fig. 22. Solution error and computational cost for $p = 2$ R^{d-1} operators on tetrahedral elements with CFL $= 0.01$, where SGFN stands for symmetry groups with facet nodes.

7.3. R^0 *operators*

Just as was done for the triangular elements in Section 6.3, the tetrahedral R^0 operators are assembled by first constructing a facet cubature rule with $p_{\text{cub}} = 2p$.

7.3.1. $p = 1$ R^0 *operators*

The facet cubature rules that are used for the tetrahedral $p = 1$ R^0 operators are the two $p = 1$ R^d operators, which are shown in Fig. 12. Fig. 23 shows the solution error for both test cases for the generated operators. For the linear convection test case, the operator with $n = 13$ and $p_{\text{cub}} = 2p = 2$, which has the same cubature rule as an operator in [30], has the lowest solution error for a given computational cost. The operator with $n = 7$ and $p_{\text{cub}} = 2p = 2$ has close to the minimum solution error for the linear convection test case and the lowest solution error for the Euler test case. The additional advantage of the $p = 7$ operator is that it has six fewer element nodes than the operator with

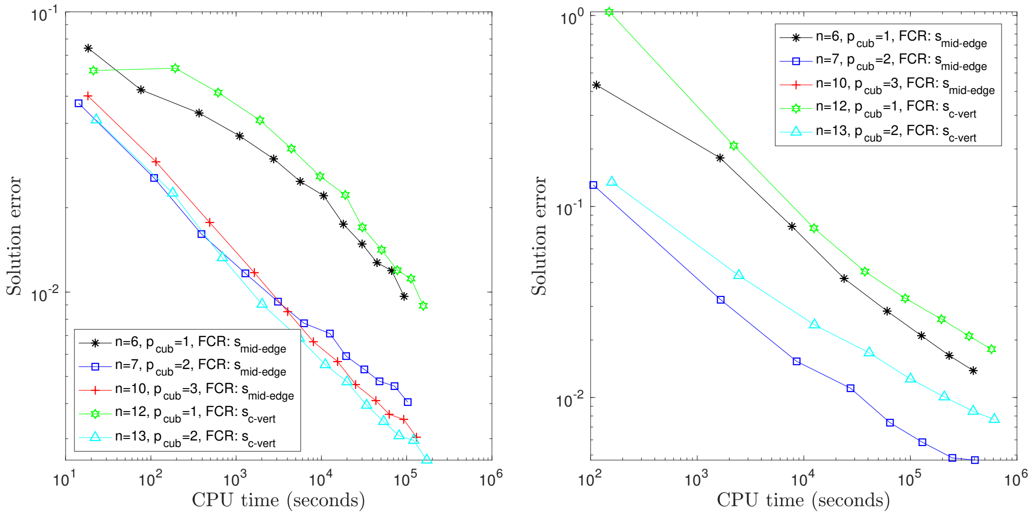

(a) Periodic linear convection test case

(b) Manufactured Euler solution test case

Fig. 23. Solution error and computational cost for $p = 1$ R^0 operators on tetrahedral elements, where FCR stands for facet cubature rule, where FCR stands for facet cubature rule.

Table 8: Possible combinations of symmetry groups for a facet cubature rule of degree four on a tetrahedral element.

ID	Element sym groups	Facet (tri) sym groups	n	Valid SBP cub rule
1	$s_{\text{face-cent}} + s_{\text{vert}} + s_{\text{c-face-vert}}$	$s_{\text{cent}} + s_{\text{vert}} + s_{\text{c-vert}}$	20	✗
2	$s_{\text{face-cent}} + s_{\text{vert}} + s_{\text{edge}}$	$s_{\text{cent}} + s_{\text{vert}} + s_{\text{c-vert}}$	20	✗
3	$s_{\text{face-cent}} + s_{\text{mid-edge}} + s_{\text{c-face-vert}}$	$s_{\text{cent}} + s_{\text{mid-edge}} + s_{\text{c-vert}}$	22	✓
4	$s_{\text{face-cent}} + s_{\text{mid-edge}} + s_{\text{edge}}$	$s_{\text{cent}} + s_{\text{mid-edge}} + s_{\text{edge}}$	22	✗
5	$s_{\text{vert}} + s_{\text{mid-edge}} + s_{\text{c-face-vert}}$	$s_{\text{vert}} + s_{\text{mid-edge}} + s_{\text{c-vert}}$	22	✓
6	$s_{\text{vert}} + s_{\text{mid-edge}} + s_{\text{edge}}$	$s_{\text{vert}} + s_{\text{mid-edge}} + s_{\text{edge}}$	22	✗
7	$2\,s_{\text{c-face-vert}}$	$2\,s_{\text{c-vert}}$	24	✓
8	$s_{\text{c-face-vert}} + s_{\text{edge}}$	$s_{\text{c-vert}} + s_{\text{edge}}$	24	✓
9	$2\,s_{\text{edge}}$	$2\,s_{\text{edge}}$	24	✗

$n = 13$. The difference in the solution error for the operator with $n = 7$ compared to the operator with $n = 13$ is $e_{\text{s,diff}} = 68\%$ and $e_{\text{s,diff}} = -39\%$ for the linear convection and Euler test cases, respectively.

7.3.2. *$p = 2$ R^0 operators*

Table 3 indicates that a cubature rule with $p_{\text{cub}} = 4$ on a triangle, which is required for a $p = 2$ R^0 operator, requires four DOF. Table 8 lists all of the combination of the symmetry groups that provide four DOF that could be used to create a facet cubature rule. Fig. 24 then shows all of the cubature rules that were found with exclusively positive weights. Fig. 25 shows the results for both test cases for all of the operators that were derived with 36 or fewer nodes using the facet cubature rules in Fig. 24. The operator with $n = 36$ and $p_{\text{cub}} = 2p = 4$ has the same cubature rule as the operator published in [30]. The operator with $n = 26$ and $p_{\text{cub}} = 2p = 4$ has the lowest solution error for both test cases. The reduction in the solution error for the $n = 26$ operator relative to the operator with $n = 36$ is $e_{\text{s,diff}} = -44\%$ and $e_{\text{s,diff}} = -68\%$ for the linear convection and Euler test cases, respectively.

7.3.3. *Summary of results*

The tetrahedral operators with the lowest solution error, the fewest element nodes, and the ones used as a reference are listed in Table 9. Once again, there is a clear benefit to increasing the degree of the cubature rule from $2p - 1$ to $2p$, but not any further. The best operators for the $p = 1$ and $p = 2$ R^d family were both previously derived and have $n = N^*_{p,3}$. Novel R^{d-1} $p = 1$ and $p = 2$ operators were constructed with lower solution errors than the best previously

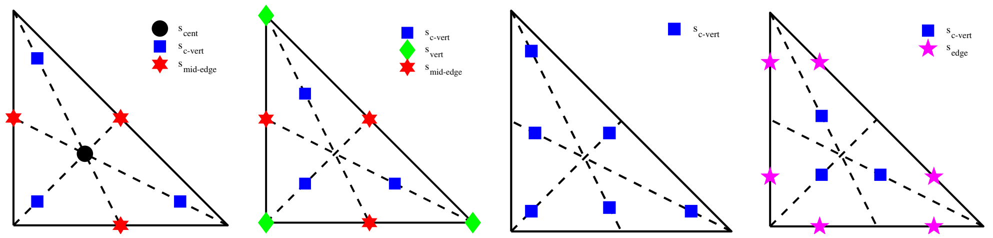

(a) ID: 3 (b) ID: 5 (c) ID: 7 (d) ID: 8

Fig. 24. Cubature rules with $p_{\text{cub}} = 4$ on triangles from Table 8 used for $p = 2$ R^0 operators on tetrahedral elements.

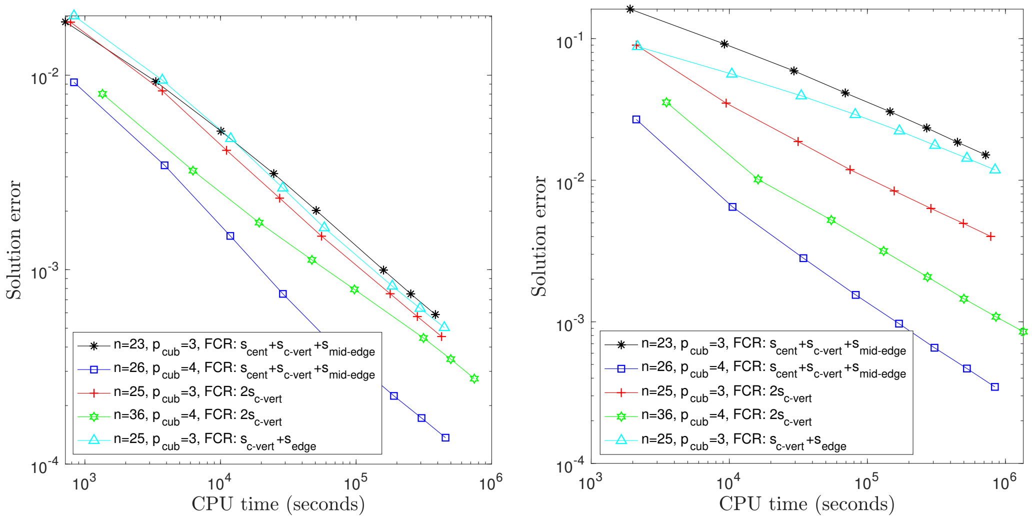

(a) Periodic linear convection test case (b) Manufactured Euler solution test case

Fig. 25. Solution error and computational cost for $p = 2$ R^0 operators on tetrahedral elements with CFL $= 0.02$, where FCR stands for facet cubature rule, where FCR stands for facet cubature rule.

Table 9: Summary of results for the tetrahedral operators, where LCE stand for linear convection equation, FCR is facet cubature rule, and where novel cub. refers to novel cubature rules used for SBP operators.

Family	p	ID	p_{cub}	$e_{\text{s,diff}}$		Diff. in n		Novel cub.
				LCE	Euler eq.	Δn	$\Delta n\%$	
R^d	1	$n = 4$	$2p = 2$	-	-	-	-	✗ [30]
	2	$n = 10$	$2p - 1 = 3$	-	-	-	-	✗ [30]
R^{d-1}	1	$n = 4$	$2p - 1 = 1$	-	-	-	-	✗ [6]
		$n = 5$	$2p = 2$	-94%	-96%	1	25%	✓
	2	$n = 11$	$2p - 1 = 3$	-	-	-	-	✗ [6]
		$n = 20$	$2p = 4$	-73%	-86%	9	82%	✓
R^0	1	$n = 13$	$2p = 2$	-	-	-	-	✗ [30]
		$n = 6$	$2p - 1 = 1$	284%	80%	-7	-54%	✓
		$n = 7$	$2p = 2$	68%	-39%	-6	-46%	✓
	2	$n = 36$	$2p = 4$	-	-	-	-	✗ [30]
		$n = 23$	$2p - 1 = 3$	114%	1130%	-13	-36%	✓
		$n = 26$	$2p = 4$	-44%	-68%	-10	-28%	✓

published operators. For the R^0 family, new operators with fewer element nodes and with lower solution errors were constructed. It is possible to construct novel R^0 operators with significantly fewer element nodes by having facet cubature rules with element nodes on the edges and vertices, which allows each element node to be on several facets.

8. Conclusions

In the construction of SBP operators it was demonstrated that R_1 needs to be constructed such that the contributions of element nodes must be the same about symmetry lines and planes. This requirement is needed such that when E_η and E_ζ are constructed by permuting E_ξ, they still have the required decomposition that involves R_1.

The optimization of free parameters in the cubature rule, in R_1 and in S_ξ was investigated. It was determined that increasing the degree of the cubature rule from $2p-1$ to $2p$ is beneficial, but there is no benefit to increasing p_{cub} any further. Next, it was determined that solving R_1 using a set of modified Moore-Penrose pseudoinverse equations provides the required structure in R_1 and returns an operator with a nearly minimized spectral radius. Finally, it was demonstrated that the optimization of free parameters in S_ξ to minimize the Frobenius norm of A is a convex optimization problem. The method used to optimize the $p = 1$ and $p = 2$ operators can be directly applied to higher order operators. The only complication that arises is constructing cubature rules of higher degrees.

Novel multidimensional operators were constructed on triangular and tetrahedral elements. In all but one case, the operator with the lowest solution error at the computational cost that was considered has $p_{\text{cub}} > 2p-1$. In all but a few cases, one operator has the lowest solution error for both test cases considered. This indicates that the best operators provide a low solution error for a variety of problems. New tetrahedral operators for the R^0 family were derived with fewer element nodes and with lower solution errors than the best previously published operators of the same family and degree. For instance, a $p = 2$ R^d operator was derived with ten fewer element nodes and with a solution error 44% to 68% lower than the best previously published operator of the same family and degree.

Appendix A. Permutation of the operators

Appendix A.1. Permutation matrices

When all the element and facet nodes are in symmetry groups, each node is mirrored to another node across a symmetry line or plane for triangular and tetrahedral elements, respectively. If a node is on a symmetry line or plane, then it mirrors itself. Permutation matrices can be created that relate nodes that are mirroring each other across symmetry lines and planes. When a matrix is left multiplied by P, its rows are permuted while if it is right multiplied by P, its columns are permuted. All permutation matrices are orthogonal and as such $\mathsf{P}^{-1} = \mathsf{P}^T$.

Given a node a, there exists a node b in the reference triangular element in Fig. 3a that satisfies the following relations for each symmetry line

$$\text{Sym \#1: } \xi_a = \eta_b, \qquad \eta_a = \xi_b, \tag{A.1}$$

$$\text{Sym \#2: } \xi_a = \xi_b, \qquad \eta_a = 1 - \xi_b - \eta_b, \tag{A.2}$$

$$\text{Sym \#3: } \xi_a = 1 - \xi_b - \eta_b, \qquad \eta_a = \eta_b, \tag{A.3}$$

where the symmetry line number comes from the number of the vertex and facet to which it is connected. Similarly, given a node a, there exists a node b in the reference tetrahedral element in Fig. 3b that satisfies the following relations for each symmetry plane

$$\text{Sym \#1: } \xi_a = \xi_b, \qquad \eta_a = \zeta_b, \qquad \zeta_a = \eta_b, \tag{A.4}$$

$$\text{Sym \#2: } \xi_a = \zeta_b, \qquad \eta_a = \eta_b, \qquad \zeta_a = \xi_b, \tag{A.5}$$

$$\text{Sym \#3: } \xi_a = \eta_b, \qquad \eta_a = \xi_b, \qquad \zeta_a = \zeta_b, \tag{A.6}$$

$$\text{Sym \#4: } \xi_a = \xi_b, \qquad \eta_a = \eta_b, \qquad \zeta_a = 1 - \xi_b - \eta_b - \zeta_b, \tag{A.7}$$

$$\text{Sym \#5: } \xi_a = \xi_b, \qquad \eta_a = 1 - \xi_b - \eta_b - \zeta_b, \qquad \zeta_a = \zeta_b, \tag{A.8}$$

$$\text{Sym \#6: } \xi_a = 1 - \xi_b - \eta_b - \zeta_b, \qquad \eta_a = \eta_b, \qquad \zeta_a = \zeta_b, \tag{A.9}$$

where the symmetry plane number comes from the number of the edge it is connected to.

Consider a triangular element with element nodes at the vertices numbered in the same order as the vertices in Fig. 3a. The permutation matrix needs to permute element nodes two and three with each other and keep element node one untouched. The permutation matrix across the first symmetry line is therefore

$$\mathsf{P}_1 = \begin{bmatrix} 1 & 0 & 0 \\ 0 & 0 & 1 \\ 0 & 1 & 0 \end{bmatrix},$$

where the subscript on the permutation matrix indicates for which symmetry line or plane it is for. Since the first symmetry line for the triangle also coincides with the line $\xi = \eta$, the permutation matrix is also denoted as $\mathsf{P}_{\xi-\eta}$. For the reference tetrahedral element in Fig. 3a, the permutation matrices that coincide with the permutation of coordinates are $\mathsf{P}_{\eta-\zeta} = \mathsf{P}_1, \mathsf{P}_{\xi-\zeta} = \mathsf{P}_2$ and $\mathsf{P}_{\xi-\eta} = \mathsf{P}_3$. Permutation matrices that are created for symmetry lines and planes have the additional property that if they are applied twice, they return the initial solution, i.e. $\mathsf{P}_i\mathsf{P}_i = \mathsf{I}$. Therefore, these permutation matrices are symmetric and $\mathsf{P}_i = \mathsf{P}_i^{-1}$. This relation does not hold for all permutation matrices.

Appendix A.2. Permuting directional operators

Section 4.1 introduced Theorem 1, which indicates that directional operators such as D_η can be created by permuting D_ξ. The proof is provided here using the permutation matrices from Appendix A.1.

Proof: Let us begin by left-multiplying the accuracy conditions from Definition 1 by $\mathsf{P}_{\xi-\eta}$:

$$\begin{aligned} \mathsf{P}_{\xi-\eta}\mathsf{D}_\xi\mathsf{V} &= \mathsf{P}_{\xi-\eta}\mathsf{V}_\xi \\ \mathsf{P}_{\xi-\eta}\mathsf{D}_\xi(\mathsf{P}_{\xi-\eta}\mathsf{P}_{\xi-\eta}^{-1})\mathsf{V} &= \mathsf{P}_{\xi-\eta}\mathsf{V}_\xi \\ (\mathsf{P}_{\xi-\eta}\mathsf{D}_\xi\mathsf{P}_{\xi-\eta})(\mathsf{P}_{\xi-\eta}\mathsf{V}) &= \mathsf{P}_{\xi-\eta}\mathsf{V}_\xi, \end{aligned} \tag{A.10}$$

where the property $\mathsf{P}_{\xi-\eta}^{-1} = \mathsf{P}_{\xi-\eta}$ was used. If the Vandermonde matrix V is created using monomial basis functions, then we have $\mathsf{V} = \xi^a\eta^b$ and $\mathsf{V}_\xi = a\xi^{a-1}\eta^b$. Left-multiplying a matrix by $\mathsf{P}_{\xi-\eta}$ permutes the solution across the line $\xi = \eta$ and thus $\mathsf{P}_{\xi-\eta}\mathsf{V} = \eta^a\xi^b$ and $\mathsf{P}_{\xi-\eta}\mathsf{V}_\xi = a\eta^{a-1}\xi^b = \mathsf{V}_\eta$. From these relations and Eq. (A.10), it is clear that $\mathsf{D}_\eta = \mathsf{P}_{\xi-\eta}\mathsf{D}_\xi\mathsf{P}_{\xi-\eta}$. This completes the proof. The proof for three-dimensional operators is analogous.

Appendix A.3. Permuting the interpolation/extrapolation operators R

Theorem 2 was presented in Section 4.1 and indicates that the interpolation/extrapolation operator for all the facets can be found by permuting the operator for the first facet. This is now proven using the permutation matrices from Appendix A.1.

Proof: We begin by considering the condition that R_2 must satisfy, which is analogous to the one for R_1:

$$\begin{aligned} \mathsf{R}_2\mathsf{V}_{\hat{\Omega}} &= \mathsf{V}_{\hat{\Gamma}_2} \\ (\mathsf{R}_1\mathsf{P}_{\mathrm{r}:1-2})\mathsf{V}_{\hat{\Omega}} &= \mathsf{V}_{\hat{\Gamma}_2}, \end{aligned} \tag{A.11}$$

where $\mathsf{P}_{\mathrm{r}:1-2} = \mathsf{P}_1\mathsf{P}_3$ from Theorem 2. The transformation to $\mathsf{V}_{\hat{\Omega}}$ caused by each permutation matrix is considered individually. If $\mathsf{V}_{\hat{\Omega}} = \xi_1^a\eta_1^b$, then $\mathsf{P}_3\mathsf{V}_{\hat{\Omega}} = (1-\xi_1-\eta_1)^a\eta_1^b$ (as per Eq. (A.3)) and $\mathsf{P}_1\mathsf{P}_3\mathsf{V}_{\hat{\Omega}} = (1-\eta_1-\xi_1)^a\xi_1^b$ (as per Eq. (A.1)). The left multiplication of $\mathsf{V}_{\hat{\Omega}}$ by $\mathsf{P}_1\mathsf{P}_3$ has created the relations $\xi_2 = 1-\xi_1-\eta_1$ and $\eta_2 = \xi_1$. A reference triangular element using ξ_1 and η_1 for the axes but ξ_2 and η_2 for the vertex coordinates is shown in Fig. A.26. Where previously there was facet *i* there is now facet *ii* with the arrow pointing from vertex *III* to vertex *I*, just like facet *ii* in Fig. 3a. Therefore, the right multiplication of R_1 by $\mathsf{P}_1\mathsf{P}_3$ causes the solution to be interpolated/extrapolated to facet *ii*, hence $\mathsf{R}_2 = \mathsf{R}_1\mathsf{P}_1\mathsf{P}_3$, which proves Theorem 2.

The proof to permute R from any other two facets for tetrahedral operators is analogous. The permutation matrices that are used to permute R between two facets depends on the direction of evaluation on the facets and in three dimensions it also depends on the starting vertex as well. The order of the evaluation used in two and three dimensions is shown in Table A.10.

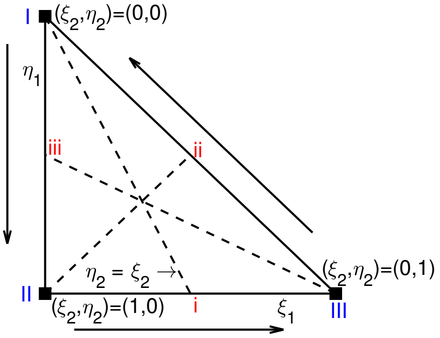

Fig. A.26. Coordinates of reference triangular element permuted by $\mathsf{P}_1\mathsf{P}_3$.

Table A.10: Order of the vertices on each facet for the reference elements shown in Fig. 3.

	Order of the vertices				
Facet no.	Triangle		Tetrahedron		
1	2	3	2	3	4
2	3	1	3	1	4
3	1	2	1	2	4
4			1	3	2

The permutation for R_1 to R_3 using the order of evaluation given in Table A.10 for a triangular element is given by

$$\mathsf{P}_{\mathrm{r}:1-3} = \mathsf{P}_1\mathsf{P}_2, \tag{A.12}$$

while the permutation of R_1 to all of the other facets for a tetrahedral operator is

$$\mathsf{P}_{\mathrm{r}:1-2} = \mathsf{P}_3\mathsf{P}_6, \tag{A.13}$$

$$\mathsf{P}_{\mathrm{r}:1-3} = \mathsf{P}_3\mathsf{P}_5, \tag{A.14}$$

$$\mathsf{P}_{\mathrm{r}:1-4} = \mathsf{P}_2\mathsf{P}_4. \tag{A.15}$$

Note that in general $\mathsf{P}_{\mathrm{r}:i-j} \neq \mathsf{P}^T_{\mathrm{r}:i-j}$, unlike $\mathsf{P}_{\xi-\eta}$ for example.

Appendix B. The need for R_1 to be symmetric

In Section 4.2 Theorem 3 was presented and the proof is provided here.

Proof: For the stability proofs E_η must also satisfy

$$\mathsf{E}_\eta = \sum_{j=1}^{N_{\hat{\mathrm{f}}}} n_{\eta,j}\mathsf{R}_j^T\mathsf{B}_j\mathsf{R}_j, \tag{B.1}$$

which can be rewritten using the permutation matrices into

$$\begin{aligned}\mathsf{E}_\eta &= \sum_{j=1}^{N_{\hat{\mathrm{f}}}} n_{\eta,j}(\mathsf{R}_1\mathsf{P}_{\mathrm{r}:1-j})^T\mathsf{B}_j(\mathsf{R}_1\mathsf{P}_{\mathrm{r}:1-j}) \\ &= \sum_{j=1}^{N_{\hat{\mathrm{f}}}} n_{\eta,j}\mathsf{P}^T_{\mathrm{r}:1-j}(\mathsf{R}_1^T\mathsf{B}_j\mathsf{R}_1)\mathsf{P}_{\mathrm{r}:1-j}.\end{aligned} \tag{B.2}$$

Table B.11: Directional normals on each facet for reference elements from Fig. 3 with cubature weights scaled to facets two and three for the triangle and facets two, three and four for the tetrahedron.

	Triangle		Tetrahedron		
Facet number (j)	$n_{\xi,j}$	$n_{\eta,j}$	$n_{\xi,j}$	$n_{\eta,j}$	$n_{\zeta,j}$
1	1	1	1	1	1
2	1	0	1	0	0
3	0	1	0	1	0
4			0	0	1

To have the term in parentheses in Eq. (B.2) be constant for each facet, the same facet cubature rule is used for each facet and the scaling that is needed for the facet cubature rule to match the length or area of the facet is included in the unit normal $n_{\eta,j}$. The unit normal for each of the facets for the triangular and tetrahedral reference elements in Fig. 3 is shown in Table B.11.

Substituting the unit normals from Table B.11 into Eqs. (5) and (B.1) gives

$$\mathsf{E}_\xi = \mathsf{R}_1^T\mathsf{B}\mathsf{R}_1 - \mathsf{P}_{\mathrm{r}:1-2}^T(\mathsf{R}_1^T\mathsf{B}\mathsf{R}_1)\mathsf{P}_{\mathrm{r}:1-2}, \tag{B.3}$$

$$\mathsf{E}_\eta = \mathsf{R}_1^T\mathsf{B}\mathsf{R}_1 - \mathsf{P}_{\mathrm{r}:1-3}^T(\mathsf{R}_1^T\mathsf{B}\mathsf{R}_1)\mathsf{P}_{\mathrm{r}:1-3}, \tag{B.4}$$

where $\mathsf{P}_{\mathrm{r}:1-1}$ is omitted since it is simply the identity matrix. The first terms in Eqs. (B.3) and (B.4) are for facet *i*, while the second terms are for facets *ii* and *iii*, respectively.

The operators E_η that are constructed from the permutation of E_ξ and from the construction of R_1 need to be identical. Therefore, Eqs. (11) and (B.4) need to return the same solution. Equating these two solutions gives

$$\begin{aligned}\mathsf{E}_\eta &= \mathsf{P}_{\xi-\eta}\mathsf{E}_\xi\mathsf{P}_{\xi-\eta}\\ \mathsf{R}_1^T\mathsf{B}\mathsf{R}_1 - \mathsf{P}_{\mathrm{r}:1-3}^T(\mathsf{R}_1^T\mathsf{B}\mathsf{R}_1)\mathsf{P}_{\mathrm{r}:1-3} &= \mathsf{P}_{\xi-\eta}\left(\mathsf{R}_1^T\mathsf{B}\mathsf{R}_1 - \mathsf{P}_{\mathrm{r}:1-2}^T(\mathsf{R}_1^T\mathsf{B}\mathsf{R}_1)\mathsf{P}_{\mathrm{r}:1-2}\right)\mathsf{P}_{\xi-\eta}.\end{aligned} \tag{B.5}$$

To facilitate the analysis, only the contributions for facet *i* are considered, which are the first terms on the LHS and RHS of Eq. (B.5).

$$\begin{aligned}\mathsf{R}_1^T\mathsf{B}\mathsf{R}_1 &= \mathsf{P}_{\xi-\eta}\left(\mathsf{R}_1^T\mathsf{B}\mathsf{R}_1\right)\mathsf{P}_{\xi-\eta}\\ &= (\mathsf{R}_1\mathsf{P}_{\xi-\eta})^T\mathsf{B}(\mathsf{R}_1\mathsf{P}_{\xi-\eta}),\end{aligned} \tag{B.6}$$

where the identity $\mathsf{P}_{\xi-\eta} = \mathsf{P}_{\xi-\eta}^T$ was used. To identify the restriction on R_1 for Eq. (B.6) to be satisfied, the LHS and RHS need to be decomposed into their individual terms. Let C_L and C_R represent the LHS and RHS of Eq. (B.6), respectively, which give

$$\mathsf{C}_L(i,j) = \sum_{k=1}^{n_f} b_k r_{k,i} r_{k,j}, \tag{B.7}$$

$$\mathsf{C}_R(i,j) = \sum_{k=1}^{n_f} b_k u_{k,i} u_{k,j}, \tag{B.8}$$

where $r_{k,i} = \mathsf{R}_1(k,i)$, $\mathsf{U} = \mathsf{R}_1\mathsf{P}_{\xi-\eta}$ and $u_{k,i} = \mathsf{U}(k,i)$.

So far, the proof has been applicable to E_η for both a triangular and tetrahedral operator. The remainder of the proof is specific to triangular elements, but the results are applicable to tetrahedral operators as well. Consider the element in Fig. B.27, which contains all of its element and facet nodes in symmetry groups, some of which are on the symmetry line $\xi = \eta$. For this operator, the matrices R_1 and U are

$$\mathsf{R}_1 = \begin{bmatrix} r_{a,1} & r_{a,2} & r_{a,3}\\ r_{b,1} & r_{b,2} & r_{b,3}\\ r_{c,1} & r_{c,2} & r_{c,3}\end{bmatrix}, \quad \mathsf{U} = \begin{bmatrix} u_{a,1} & u_{a,2} & u_{a,3}\\ u_{b,1} & u_{b,2} & u_{b,3}\\ u_{c,1} & u_{c,2} & u_{c,3}\end{bmatrix}.$$

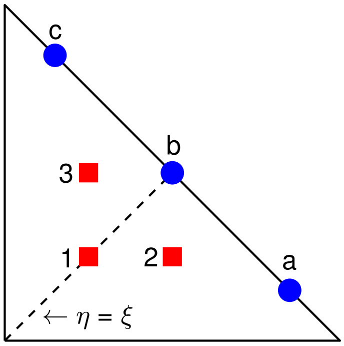

Fig. B.27. Example of a triangular element with an element and facet cubature rule.

Since U is constructed from permuting R_1, their entries are related

$$r_{k,1} = u_{k,1}, r_{k,2} = u_{k,3}, r_{k,3} = u_{k,2}, \quad \forall k \in \{a, b, c\}. \tag{B.9}$$

Unfortunately, these relations are insufficient to ensure that $\mathsf{C}_L = \mathsf{C}_R$. The set of equations that needs to be satisfied is

$$\mathsf{C}_L(i, j) - \mathsf{C}_R(i, j) = \sum_{k=1}^{n_f} b_k \left(r_{k,i} r_{k,j} - u_{k,i} u_{k,j} \right) = 0, \quad \forall i, j \in \{1, 2, \ldots, n\}. \tag{B.10}$$

Since all of the facet nodes are in symmetry groups, the facet cubature rule has the same weights for all of the nodes in the same symmetry group. For an operator with a linear facet and its nodes numbered consecutively, such as the one in Fig. B.27, the relations $b_k = b_{-k}$, where $b_k = \mathsf{B}(k, k)$ and $b_{-k} = \mathsf{B}(n_f + 1 - k, n_f + 1 - k)$ and $-k = n_f + 1 - k$ are used. This relation allows Eq. (B.10) to be rewritten in the form

$$\begin{aligned} \mathsf{C}_L(i, j) - \mathsf{C}_R(i, j) = &\sum_{k=\{a,c\}} b_k \left(\left(r_{k,i} r_{k,j} + r_{-k,i} r_{-k,j} \right) - \left(u_{k,i} u_{k,j} + u_{-k,i} u_{-k,j} \right) \right) \\ &+ \sum_{k=\{b\}} b_k \left(r_{k,i} r_{k,j} - u_{k,i} u_{k,j} \right) = 0 \quad \forall i, j \in \{1, 2, \ldots, n\}. \end{aligned} \tag{B.11}$$

The first summation term on the RHS of Eq. (B.11) is for the facet nodes in the symmetry group $\mathrm{s}_{\text{c-vert}}$, while the second summation on the RHS is for the facet centroid s_{cent}. To ensure that Eq. (B.11) is satisfied, each term in the summations is set to zero and thus

$$\left(r_{k,i} r_{k,j} + r_{-k,i} r_{-k,j} \right) - \left(u_{k,i} u_{k,j} + u_{-k,i} u_{-k,j} \right) = 0 \quad \forall i, j \in \{1, 2, \ldots, n\}, k \in \{a, c\} \tag{B.12}$$

$$r_{k,i} r_{k,j} - u_{k,i} u_{k,j} = 0 \quad \forall i, j \in \{1, 2, \ldots, n\}, k \in \{b\}. \tag{B.13}$$

To satisfy Eq. (B.12), the following relations can be used:

$$r_{k,i} = u_{-k,i}, \quad r_{-k,i} = u_{k,i} \quad \forall i = \{1, 2, \ldots, n\}, k \in \{a, c\}. \tag{B.14}$$

When the relations from Eqs. (B.14) and (B.9) are applied, this results in $r_{a,2} = r_{c,3}$, $r_{c,2} = r_{a,3}$ and $r_{a,1} = r_{c,1}$. These results are shown in Fig. 4a. Meanwhile, to satisfy Eq. (B.13), the relations that are used are

$$r_{k,i} = u_{k,i} \quad \forall i \in \{1, 2, \ldots, n\}, k \in \{b\}. \tag{B.15}$$

The relations from Eqs. (B.15) and (B.9) gives $r_{2,b} = r_{3,b}$, which is shown in Fig. 4b. This completes the proof.

Appendix C provides modified equations that can be used to create the matrix R_1 with the required properties such that when E_η and E_ζ are created by permuting E_ξ, they have the proper decomposition that involves R_1.

Appendix C. Equations to Create a Symmetric R_1

The use of Eq. (4) does not guarantee that the contributions of element nodes are symmetric about symmetry lines and planes. The consequence of this is that if E_ξ is permuted to calculate the other directional surface integrals, E_η and E_ζ might not have the required decomposition into R_1. The stability proofs presented in [7] require that the directional surface integrals have a particular decomposition into R_1 to ensure that the energy is bounded. It may be possible to prove stability without the decomposition of E_ξ and the other directional surface integrals into R_1, but this has not been demonstrated.

Appendix C.1. Triangular elements

In order to ensure that the interpolation/extrapolation of the solution from the element nodes to the facet centroid, element node b in Fig. B.27, is symmetric when all of the element nodes are in symmetry groups, Eq. (4) is modified to be in the form

$$\mathsf{R}_1(b,:) = \frac{\mathsf{I} + \mathsf{P}_{\xi-\eta}}{2}\mathsf{V}_{\hat{\Gamma}_1}(b,:)(\mathsf{V}_{\hat{\Omega}})^\dagger. \tag{C.1}$$

The term $(\mathsf{I} + \mathsf{P}_{\xi-\eta})/2$ ensures that the contribution across the symmetry line $\xi = \eta$ is symmetric since it takes the average of the solution given by Eq. (4) and the solution permuted across the symmetry line. When $n = N^*_{p,d}$, there are no free parameters in R_1 and therefore both Eqs. (4) and (C.1) return the same solution. However, when $n > N^*_{p,d}$, Eqs. (4) and (C.1) are not guaranteed to return the same solution.

The interpolation/extrapolation solution for nodes a and c in Fig. B.27 can be calculated for one node first and then the solution can be permuted to the other node. For example, the solution for element node a can be found with

$$\mathsf{R}_1(a,:) = \mathsf{V}_{\hat{\Gamma}_1}(a,:)(\mathsf{V}_{\hat{\Omega}})^\dagger, \tag{C.2}$$

and then the solution for element node c is calculated with

$$\mathsf{R}_1(c,:) = \mathsf{R}_1(a,:)\mathsf{P}_{\xi-\eta}. \tag{C.3}$$

Appendix C.2. Tetrahedral elements

In order to find the symmetric solution for the interpolation/extrapolation to the s_{cent} facet node on a tetrahedral element, node a in Fig. 5b, the following equation can be used:

$$\mathsf{R}_1(a,:) = \frac{\mathsf{I} + \mathsf{P}_{\xi-\eta} + \mathsf{P}_{\xi-\zeta}(\mathsf{I} + \mathsf{P}_{\xi-\eta}) + \mathsf{P}_{\eta-\zeta}(\mathsf{I} + \mathsf{P}_{\xi-\eta})}{6}\mathsf{V}_{\hat{\Gamma}_j}(a,:)(\mathsf{V}_{\hat{\Omega}})^\dagger, \tag{C.4}$$

The interpolation/extrapolation for node b_1 in Fig. 5b can be found from

$$\mathsf{R}_1(b_1,:) = \frac{\mathsf{I} + \mathsf{P}_{\eta-\zeta}}{2}\mathsf{V}_{\hat{\Gamma}_j}(b_1,:)(\mathsf{V}_{\hat{\Omega}})^\dagger, \tag{C.5}$$

and the solutions for nodes b_2 and b_3 are then calculated from

$$\mathsf{R}_1(b_2,:) = \mathsf{R}_1(b_1,:)\mathsf{P}_{\xi-\eta}, \tag{C.6}$$

$$\mathsf{R}_1(b_3,:) = \mathsf{R}_1(b_1,:)\mathsf{P}_{\xi-\zeta}. \tag{C.7}$$

For the facet nodes in the symmetry group $\mathrm{s}_{\text{c-edge}}$, such as node c_1 in Fig. 5b, the solution can be calculated as

$$\mathsf{R}_1(c_1,:) = \mathsf{V}_{\hat{\Gamma}_j}(c_1,:)(\mathsf{V}_{\hat{\Omega}})^\dagger, \tag{C.8}$$

and for the other nodes in the symmetry group the solutions are calculated using the following equations:

$$\mathsf{R}_1(c_2,:) = \mathsf{R}_1(c_1,:)\mathsf{P}_{\eta-\zeta}, \tag{C.9}$$

$$\mathsf{R}_1(c_3,:) = \mathsf{R}_1(c_1,:)\mathsf{P}_{\xi-\zeta}\mathsf{P}_{\xi-\eta}, \tag{C.10}$$

$$\mathsf{R}_1(c_4,:) = \mathsf{R}_1(c_1,:)\mathsf{P}_{\eta-\zeta}, \tag{C.11}$$

$$\mathsf{R}_1(c_5,:) = \mathsf{R}_1(c_1,:)\mathsf{P}_{\xi-\eta}, \tag{C.12}$$

$$\mathsf{R}_1(c_6,:) = \mathsf{R}_1(c_1,:)\mathsf{P}_{\xi-\zeta}. \tag{C.13}$$

Appendix D. System of linear equations for S_ξ

The equations that need to be satisfied for the accuracy conditions can be rewritten as a linear system of equations. This system of equations can then be used along with the objective function in Section 5.5 to minimize the Frobenius norm of A. The linear system of equations is in the form $\mathsf{C}\boldsymbol{s}_{\text{vec}} = \boldsymbol{d}$, where the matrix C is of size $n_{\mathsf{S}_\xi \text{ind eq}} \times n_{\mathsf{S}_\xi \text{DOF}}$, the free parameters of S_ξ are held in the vector $\boldsymbol{s}_{\text{vec}}$, and $\boldsymbol{d}$ is a vector of length $n_{\mathsf{S}_\xi \text{ind eq}}$.

In order to create the system of linear equations the DOF in S_ξ need to be related to the entries in s_{vec} with a single index notation, which is defined as $k = (j-2)(j-1)/2 + i, i < j$. For an operator with four element nodes we have

$$\mathsf{S}_\xi = \underbrace{\begin{bmatrix} 0 & s_{1,2} & s_{1,3} & s_{1,4} \\ -s_{1,2} & 0 & s_{2,3} & s_{2,4} \\ -s_{1,3} & -s_{2,3} & 0 & s_{3,4} \\ -s_{1,4} & -s_{2,4} & -s_{3,4} & 0 \end{bmatrix}}_{(i,j)\text{ notation}} = \underbrace{\begin{bmatrix} 0 & s_1 & s_2 & s_4 \\ -s_1 & 0 & s_3 & s_5 \\ -s_2 & -s_3 & 0 & s_6 \\ -s_4 & -s_5 & -s_6 & 0 \end{bmatrix}}_{(k)\text{ notation}}.$$

and the vector of DOF is $\boldsymbol{s}_{\text{vec}} = [s_1, s_2, \ldots, s_{n(n-1)/2}]^T$. The LHS and RHS of Eq. (18) are

$$\text{LHS}_1 = \mathsf{V}^T \mathsf{S}_\xi \mathsf{V}, \tag{D.1}$$

$$\text{LHS}_1(a,b) = \sum_{i=2}^{n} \sum_{j=1}^{i-1} s_{i,j}(v_{i,a}v_{j,b} - v_{j,a}v_{i,b}), \tag{D.2}$$

$$\text{RHS}_1 = \frac{1}{2}(\mathsf{V}^T \mathsf{H} \mathsf{V}_\xi - \mathsf{V}_\xi^T \mathsf{H} \mathsf{V}), \tag{D.3}$$

where the notation $v_{i,a} = \mathsf{V}(i,a)$ is used. The upper triangular section of S_ξ contributes $s_{i,j}v_{i,a}v_{j,b}$, while the lower triangular section contributes the term $-s_{i,j}v_{j,a}v_{i,b}$ to the LHS. The LHS and RHS are rewritten as a system of linear equations as follows:

$$\mathsf{C}(m,k) = v_{i,a}v_{j,b} - v_{j,a}v_{i,b}, \tag{D.4}$$

$$\boldsymbol{d}(m) = \text{RHS}_1(a,b), \tag{D.5}$$

where m is a single index notation in the form $m = (a-2)(a-1)/2 + b$. The LHS and RHS of Eq. (17) are

$$\text{LHS}_2 = \mathsf{W}^T \mathsf{S}_\xi \mathsf{V}, \tag{D.6}$$

$$\text{LHS}_2(a,b) = \sum_{i=2}^{n} \sum_{j=1}^{i-1} s_{i,j}(w_{i,a}v_{j,b} - w_{j,a}v_{i,b}), \tag{D.7}$$

$$\text{RHS}_2 = \mathsf{W}^T \mathsf{H} \mathsf{V}_\xi - \frac{1}{2}\mathsf{W}^T \mathsf{E}_\xi \mathsf{V}. \tag{D.8}$$

The equations from Eq. (17), which are only needed when $n > N^*_{p,d}$, are added to the system of linear equations

$$\mathsf{C}(m_2,k) = w_{i,a}v_{j,b} - w_{j,a}v_{i,b}, \tag{D.9}$$

$$\boldsymbol{d}(m_2) = \text{RHS}_2(a,b), \tag{D.10}$$

where $m_2 = (a-1)N^*_{p,d} + b + N^*_{p,d}(N^*_{p,d} - 1)/2$. The contribution of $N^*_{p,d}(N^*_{p,d} - 1)/2$ is added since this is the number of equations from Eq. (16). One solution to the system of linear equations is

$$\boldsymbol{s}_{\text{vec}} = \mathsf{C}^\dagger \boldsymbol{d}, \tag{D.11}$$

where the Moore-Penrose pseudoinverse is indicated by $(\cdot)^\dagger$. Alternatively, Section 5.5 presents a method to solve a convex optimization problem to solve for the values of S_ξ with the minimum Frobenius norm of A.

Acknowledgments

The financial support provided by the National Sciences and Engineering Research Council of Canada and the Government of Ontario through the Ontario Graduate Scholarship is recognized. The authors are thankful for the computational resources provided by Compute Canada as well as the insight from Prof. Masayuki Yano.

References

[1] D. C. Del Rey Fernández, J. E. Hicken, D. W. Zingg, Review of summation-by-parts operators with simultaneous approximation terms for the numerical solution of partial differential equations, Computers & Fluids 95 (2014) 171–196.

[2] M. Svärd, J. Nordström, Review of summation-by-parts schemes for initial–boundary-value problems, Journal of Computational Physics 268 (2014) 17–38. `doi:10.1016/j.jcp.2014.02.031`.

[3] M. Svärd, On coordinate transformations for summation-by-parts operators, Journal of Scientific Computing 20 (1) (2004) 29–42.

[4] D. C. Del Rey Fernández, P. D. Boom, M. H. Carpenter, D. W. Zingg, Extension of Tensor-Product Generalized and Dense-Norm Summation-by-Parts Operators to Curvilinear Coordinates, Journal of Scientific Computing 80 (3) (2019) 1957–1996. `doi:10.1007/s10915-019-01011-3`.

[5] D. C. Del Rey Fernández, P. D. Boom, D. W. Zingg, A generalized framework for nodal first derivative summation-by-parts operators, Journal of Computational Physics 266 (2014) 214–239.

[6] J. E. Hicken, D. C. Del Rey Fernández, D. W. Zingg, Multidimensional Summation-by-Parts Operators: General Theory and Application to Simplex Elements, SIAM Journal on Scientific Computing 38 (4) (2016) A1935–A1958. `doi:10.1137/15M1038360`.

[7] D. C. Del Rey Fernández, J. E. Hicken, D. W. Zingg, Simultaneous Approximation Terms for Multi-dimensional Summation-by-Parts Operators, Journal of Scientific Computing 75 (1) (2018) 83–110. `doi:10.1007/s10915-017-0523-7`.

[8] J. E. Hicken, D. W. Zingg, Summation-by-parts operators and high-order quadrature, Journal of Computational and Applied Mathematics 237 (1) (2013) 111–125. `doi:10.1016/j.cam.2012.07.015`.

[9] S. C. Chapra, R. P. Canale, Numerical Methods for Engineers, seventh edition Edition, McGraw-Hill Education, New York, NY, 2015.

[10] R. Cools, Advances in multidimensional integration, Journal of Computational and Applied Mathematics 149 (1) (2002) 1–12.

[11] M. A. Taylor, B. A. Wingate, L. P. Bos, A Cardinal Function Algorithm for Computing Multivariate Quadrature Points, SIAM Journal on Numerical Analysis 45 (1) (2007) 193–205. `doi:10.1137/050625801`.

[12] D. M. Williams, L. Shunn, A. Jameson, Symmetric quadrature rules for simplexes based on sphere close packed lattice arrangements, Journal of Computational and Applied Mathematics 266 (2014) 18–38. `doi:10.1016/j.cam.2014.01.007`.

[13] F. D. Witherden, P. E. Vincent, On the identification of symmetric quadrature rules for finite element methods, Computers & Mathematics with Applications 69 (10) (2015) 1232–1241. `doi:10.1016/j.camwa.2015.03.017`.

[14] L. Zhang, T. Cui, H. Liu, A set of symmetric quadrature rules on triangles and tetrahedra, Journal of Computational Mathematics 27 (1) (2009) 89–96.

[15] Y. Liu, M. Vinokur, Exact Integrations of Polynomials and Symmetric Quadrature Formulas over Arbitrary Polyhedral Grids, Journal of Computational Physics 140 (1998) 122–147.

[16] S. J. Smith, Lebesgue constants in polynomial interpolation, in: Annales Mathematicae et Informaticae, Vol. 33, Eszterházy Károly College, Institute of Mathematics and Computer Science, 2006, pp. 1787–5021.

[17] P. Diener, E. N. Dorband, E. Schnetter, M. Tiglio, Optimized high-order derivative and dissipation operators satisfying summation by parts, and applications in three-dimensional multi-block evolutions, Journal of Scientific Computing 32 (1) (2007) 109–145.

[18] F. D. Witherden, P. E. Vincent, An Analysis of Solution Point Coordinates for Flux Reconstruction Schemes on Triangular Elements, Journal of Scientific Computing 61 (2) (2014) 398–423. `doi:10.1007/s10915-014-9832-2`.

[19] K. Mattsson, M. Almquist, M. H. Carpenter, Optimal diagonal-norm SBP operators, Journal of Computational Physics 264 (2014) 91–111.

[20] A. L. Marchildon, D. W. Zingg, Optimization of Multi-dimensional Summation-by-Parts Operators, in: AIAA 2019-2953, American Institute of Aeronautics and Astronautics, Dallas, Texas, 2019. `doi:10.2514/6.2019-2953`.

[21] K. J. Mattalo, D. W. Zingg, Multidimensional Diagonal-Norm Summation-by-Parts Operators on Quadrilateral Elements, in: AIAA 2019-2954, American Institute of Aeronautics and Astronautics, Dallas, Texas, 2019. `doi:10.2514/6.2019-2954`.

[22] H. T. Huynh, A Flux Reconstruction Approach to High-Order Schemes Including Discontinuous Galerkin Methods, in: AIAA 2007-4079, American Institute of Aeronautics and Astronautics, Miami, FL, 2007. `doi:10.2514/6.2007-4079`.

[23] F. D. Witherden, J. S. Park, P. E. Vincent, An Analysis of Solution Point Coordinates for Flux Reconstruction Schemes on Tetrahedral Elements, Journal of Scientific Computing 69 (2) (2016) 905–920. `doi:10.1007/s10915-016-0204-y`.

[24] T. Chen, C.-W. Shu, Entropy stable high order discontinuous Galerkin methods with suitable quadrature rules for hyperbolic conservation laws, Journal of Computational Physics 345 (2017) 427–461. `doi:10.1016/j.jcp.2017.05.025`.

[25] N. Derzko, A. Pfeffer, Bounds for the Spectral Radius of a Matrix, Mathematics of Computation 19 (89) (1965) 62–67.

[26] J. Chan, D. C. Del Rey Fernández, M. H. Carpenter, Efficient entropy stable Gauss collocation methods, arXiv:1809.01178 [math] (Sep. 2018). `arXiv:1809.01178`.

[27] S. C. Spiegel, H. T. Huynh, J. R. DeBonis, A Survey of the Isentropic Euler Vortex Problem using High-Order Methods, in: 22nd AIAA Computational Fluid Dynamics Conference, American Institute of Aeronautics and Astronautics, Dallas, TX, 2015. `doi:10.2514/6.2015-2444`.

[28] J. Crean, J. E. Hicken, D. C. Del Rey Fernández, D. W. Zingg, M. H. Carpenter, Entropy-stable summation-by-parts discretization of the Euler equations on general curved elements, Journal of Computational Physics 356 (2018) 410–438. `doi:10.1016/j.jcp.2017.12.015`.

[29] L. Friedrich, D. C. Del Rey Fernández, A. R. Winters, G. J. Gassner, D. W. Zingg, J. Hicken, Conservative and Stable Degree Preserving SBP Operators for Non-conforming Meshes, Journal of Scientific Computing 75 (2) (2018) 657–686. `doi:10.1007/s10915-017-0563-z`.

[30] D. Del Rey Fernández, J. Crean, M. Carpenter, J. Hicken, Staggered-grid entropy-stable multidimensional summation-by-parts discretizations on curvilinear coordinates, Journal of Computational Physics (accepted) (Apr. 2019). `doi:10.1016/j.jcp.2019.04.029`.